Journal of Power Sources 585 (2023) 233635

Contents lists available at ScienceDirect

Journal of Power Sources

journal homepage: www.elsevier.com/locate/jpowsour

Diesel operated combined heat and power SOFC system: SOFC characterization and proof of concept

Michael Höber [a,*], Benjamin Königshofer [a], Pavle Boškoski [b], Christoph Hochenauer [a], Vanja Subotić [a]

[a] Institute of Thermal Engineering, Graz University of Technology, Inffeldgasse 25/B, Graz, 8010, Styria, Austria
[b] Jožef Stefan Institute, Jamova Cesta 39, Ljubljana, 1000, Slovenia

HIGHLIGHTS

- Development and proof of concept of a diesel operated solid oxide fuel cell system.
- Fuel cell system operation with steam and auto-thermally reformed diesel.
- Electrochemical analysis of a 30 cell stack directly operated with reformed diesel.
- Measured efficiency potential of a 30 cell stack operated with reformed diesel.

ARTICLE INFO

Keywords:
Solid oxide fuel cell (SOFC)
Diesel reforming
Combined heat and power plant
Electrochemical analysis

ABSTRACT

The high volumetric energy density and easy storage capability of liquid hydrocarbons such as bio-diesel or diesel are needed for power generation in several applications such as ships and isolated or rural areas which only have limited access to other power grids. Solid oxide fuel cells (SOFCs) can in theory utilize such fuels in a high efficient manner, which could reduce greenhouse gas emissions and energy demand. However, SOFC systems able to directly utilize diesel are rather complex to design and monitor, leading to several possible causes of system lifetime reduction. To avoid an enhanced reduction of the system lifetime, the operating conditions of all components must be optimized and monitored in detail. However, detailed monitoring and identification of the cause of performance loss are challenging using conventional system monitoring methods. Therefore, here we (i) show the concept and characterization of a SOFC system operating under steam- and auto-thermal diesel reforming conditions, (ii) demonstrated the applicability of advanced methods to monitor complex SOFC systems, which are applied on the 30 cell SOFC stack during system operation and (iii) analyzed the efficiency potential of the SOFC within the developed system. The results present in this work are favorable to accelerate commercialization.

1. Introduction

Increasing global energy demand and the necessity to reduce greenhouse gas emissions are opposing behaviors that challenge today's society. The increasing share of sustainable energy sources is the major step to reduce greenhouse gas emissions, but with increasing electric energy from wind and solar power some challenges still remain. The generated electrical energy is challenging to store and release on demand in large quantities. Hence, several possibilities to store and release large quantities of electrical energy have been investigated including: (i) mechanical, (ii) electrochemical, (iii) electrical, (iv) thermochemical, (v) chemical, and (vi) thermal energy storage technologies [1]. One promising future energy storage technology could be solar fuels. Solar fuels are based on hydrogen and carbon monoxide, which can be further processed to ammonia, or other hydrocarbons [2]. Solar fuels can be directly produced from sunlight by using photocatalysis [3], photoelectrocatalysis, and thermochemical conversion [4]. Other ways of solar fuel production include fuel production from biomass and electrolysis powered by a photovoltaic power station [4]. However, the direct use of sunlight to produce hydrogen suffers from efficiencies mostly below 10% [5] whereas the utilization of solar electrical energy in a high efficient solid oxide electrolyzer (SOE) might be more promising. SOEs are able to generate not only hydrogen but also carbon monoxide or mixtures of both, which can be used to generate fuels via the Fischer–Tropsch process. Demonstrated

* Corresponding author.
E-mail address: michael.hoeber@tugraz.at (M. Höber).

https://doi.org/10.1016/j.jpowsour.2023.233635
Received 28 July 2023; Received in revised form 8 September 2023; Accepted 11 September 2023
Available online 20 September 2023

efficiencies of SOE operation combined with Fischer–Tropsch synthesis are already up to 57.2% [6]. Another upcoming energy storage technology are batteries, with lithium-ion batteries as most promising technology due to their relatively high energy density, operating voltages and fast charge rates compared to other batteries [7,8]. Due to the critical material lithium, other battery types are also investigated for large energy storage systems such as potassium based batteries [8], sodium based batteries [9,10], and vanadium redox flow batteries [11]. However, the low volumetric energy density of batteries or hydrogen is challenging for space or weight critical applications [12,13]. Such applications can be ships [14], aircraft [15], or locations without good connections to the gas and/or electricity grid due to their for example geographic locations [16]. Stand-alone high efficient heat and power generators might be therefore especially useful for greenhouses and rural buildings. A high efficient and environmentally friendly energy converter for fuels with relatively high volumetric energy densities such as liquid hydrocarbons or ammonia is needed. An energy converter with promising high efficiencies and no NOx emissions even for ammonia utilization [17] is the solid oxide fuel cell (SOFC). The SOFC has a high fuel flexibility and is able to utilize hydrogen, ammonia, and hydrocarbons with high electrical efficiencies [18–20]. To use liquid hydrocarbons such as bio-fuels or conventional liquid hydrocarbons in SOFCs, sufficient fuel pretreatment, e.g. by reforming, is required because the direct decomposition of hydrocarbons in the SOFC can lead to severe and fast degradation of the fuel electrode [21–24].

The fuel pretreatment consists of at least a fuel reformer, but can also include water gas shift (WGS) reactors, desulphurization, CO purification, and CO_2 capture chambers [24]. Steam reforming of diesel without further reactors was successfully tested for 100 h with more than 70% H_2 in the dry reformer off gas [25]. Coking of the walls in the fuel mixing and evaporation zones was observed in [26], marking the necessity of good fuel evaporation. Another diesel reforming type, partial oxidation (POx), was tested with around 25% H_2 in the dry reformer off gas [27]. The combination of partial oxidation and steam reforming is called auto-thermal reforming. It delivers relatively high H_2 outputs without the need of continuous external heating. Auto-thermal reactors seem to be the reforming of choice if it comes to application for fuel cell/SOFC driven power supply units [28,29]. Auto-thermal reforming without other reactors is intensively investigated by Pasel et al. [23,30–32] with close to 40% H_2 in the dry reformer off gas. Potemkin et al. [33] reached around 30% H_2 in the dry reformer off gas. A more complex fuel pretreatment system consisting of an auto-thermal reformer, water gas shift reactor, and fuel cell off-gas burner to recover heat showed around 42% H_2 in the dry WGS reactor off gas [34]. However, hydrogen output or conversion performance of catalysts can decrease if catalysts degrade due to several mechanisms such as carbon deposition [21,26,33] or poisoning with trace compounds [35]. Re-oxidation of non-noble metal catalysts, such as Ni, could also lead to catalyst degradation. Catalysts used for diesel reforming are mostly metal based such as Pt and Rh [25,32–34] or Ni [26]. A review of catalyst materials for diesel reforming is given in [28]. Direct coupling of the mentioned fuel pretreatment systems with SOFCs seems to be suitable since SOFCs are able to directly utilize H_2, CO, and CH_4, which are the main outputs of the reforming processes. However, if SOFCs are directly supplied with reformed diesel, several possibilities for performance loss of SOFCs still remain. Such possibilities are (i) solid C deposition [21,36], (ii) Ni re-oxidation [37], (iii) poisoning of the fuel electrode by fuel trace compounds such as sulfur, chlorine, or other impurities [38–40] and (iv) damages due to thermal stresses caused by reforming reactions taking place on the fuel electrode [41,42]. A detailed review of degradation mechanisms for SOFCs can be found in [43]. Due to the possibility of degradation of diesel operated SOFC system components, a detailed monitoring is necessary. The detailed monitoring and early detection and identification of degradation mechanisms could help to change operating conditions insitu, limit early performance loss, and prolong the lifetime of the system. For this purpose, the temperature profile along the reformer catalyst can be measured and the SOFC can be monitored by measuring the voltage and applying electrochemical impedance spectroscopy (EIS) measurements. Shifts in the temperature profile along the reformer can indicate catalyst deactivation, but cannot give information about the type of degradation [26]. More advanced monitoring methods for catalysts are already reported, but are often challenging to implement [44–47]. Voltage monitoring of SOFCs is often applied, but can also just give limited information about the degradation mechanism. In contrast, EIS measurements and its advanced tool distribution of relaxation times (DRT) are able to link observed degradation phenomena to single processes. In addition, results of EIS measurements can characterize the performance of the SOFC and the applied operating conditions. However, to interpret EIS and DRT results, knowledge of the general operating condition and previous conducted characterizations are necessary. In case of diesel operated SOFC systems, only limited information of influences on EIS data is available. To the authors best knowledge, EIS measurements were only conducted for single cells for diesel or similar fuels, as listed in the following. Lo Faro et al. investigated operation of button cells, with an area of 2.5 cm^2, with a coupled n-dodecane steam reformer by EIS and polarization curve measurements [21,48]. A SOFC with an area of 50 × 50 mm^2 was characterized with EIS and polarization curve measurements with an auto-thermal reformed biofuel surrogate in [49]. Direct operation of a low temperature SOFC with a 3.9% iso-octane air mixture was investigated by EIS and polarization curve measurements in [50]. Real diesel operated systems seem to be only reportedly monitored by voltage and power measurements. One example is an auxiliary power unit (APU) consisting of a 30 cell stack in combination with a POx reformer. The APU was found to deliver 420 W during a 4 h stable operation, but only temperatures and the stack voltage are presented [51]. In [22], the same APU is tested with focus on monitoring the reformer (temperature distribution and gas composition), but only the system net power and stack temperature are shown as characteristics for the SOFC. An adiabatic reformer SOFC system with 2 stack modules is tested in [52]. The results only show stable operation of the stack module for 1 h and 15 min by monitoring the stack voltages at a constant current. Based on this work, Nehter et al. presented the operation of a 50 kW diesel operated SOFC system for nearly 2 h and 30 min. The SOFC operation was reportedly monitored by voltage, power, and fuel utilization [14]. Operation of an APU system for heavy duty trucks is demonstrated in [53,54] without applying advanced online monitoring techniques such as electrochemical impedance spectroscopy to determine the state of health of the SOFC. An unstable voltage and a fast voltage decrease can be observed in [54], but no information about the cause is available.

In this study, we show the development and testing of a research friendly diesel operated SOFC system. The diesel reforming unit is investigated in preliminary diesel reforming tests to identify safe and suitable operating conditions for the reforming process. After identifying suitable diesel reforming conditions, the system with a 30 cell SOFC stack is operated with two different diesel reforming strategies, which are both characterized. The characterization measurements include voltage monitoring, SOFC off gas analysis, EIS measurements and evaluation by applying the DRT method. We successfully applied EIS measurements and DRT analysis, which is the first reported time for large SOFC stacks in system application, to the best of the authors knowledge. The gained data from EIS and DRT helped to identify a not ideal operating condition, which shows that high data quality is achieved even if several system components might influence the measurement. The presented results show the applicability of advanced measurement techniques such as EIS to monitor even complex SOFC systems. These advanced measurement techniques enable precise system monitoring and can provide insights into the systems state of health. This offers a possibility to apply appropriate counteractions and thus control the system operation stability, increase its reliability,

and lifetime. In addition, the presented system is a first step towards a stand-alone combined heat and power SOFC system operated with liquid hydrocarbons with all necessary infrastructure already available. Such systems are gaining more and more attention to decentralize the power supply without high losses in efficiency [55,56]. Therefore, the developed system may be useful to further investigate online monitoring of systems and operation of SOFCs with liquid hydrocarbons. However, still improvements especially for online monitoring and operating point characterization have to be done. The results shown in this study give detailed information about the system behavior under different operating conditions, occurring changes, and their impact on EIS and DRT results. In addition, an efficiency analysis and discussion is done to present the capabilities of SOFC systems operated with liquid hydrocarbons.

2. Experimental

This section is about the design of the diesel operated SOFC system, the used components, and testing conditions. It is split into 3 separate parts: (i) the design and description of the developed SOFC system, (ii) the tested SOFC stack, and (iii) the applied testing conditions.

2.1. Diesel operated SOFC system design

Within this section, the system to operate the 30 cell SOFC stack with auto-thermally reformed diesel is described. The systems piping and instrumentation diagram (P&ID) scheme with most sensors and actuators is shown in Fig. 1(a). The presented system is designed in a way that temperatures of the mixing chamber, reformer, SOFC stack, and catalytic burner are easily controllable and the components are easily exchangeable. Due to this design decision, it should be possible to gain detailed measurements and study different fuels, catalysts and SOFC stacks with the overall same system. Unfortunately, the reachable net system efficiency is reduced by the more modular and research friendly design. A picture of the built system is shown in Fig. 1(b). The different sections marked in Fig. 1(b) show the fuel mixing and evaporation chamber (1), the reformer (2), the furnace in which the SOFC stack is placed (3), the electric load and EIS impedance measurement equipment (4), the control cabinet, (5) and the heat buffer storage (6), which is integrated in a heating circuit to be able to simulate the use of the exhaust gas heat.

The main components of the presented diesel operated SOFC system are the (i) fuel (diesel) supply, (ii) steam supply, (iii) air supply, (iv) fuel mixing and evaporation chamber, (v) reformer, (vi) SOFC stack, (vii) catalytic burner, and (viii) gas-water heat exchanger. In addition, a hydrogen supply is installed to prevent damage of the catalyst and/or the SOFC stack due to a steam or fuel supply malfunction. In the presented tests, hydrogen is also used to heat up the system and reduce the catalyst and the stack. During switching to diesel operation, the hydrogen supply is switched off. The hydrogen supply line of the system consists of a hydrogen storage (bottle containing compressed hydrogen and a pressure reducer), a ball valve, a ball-flow meter where the hydrogen flow is set to 2 slpm, and a magnetic valve to enable automated switching on or off of the hydrogen supply.

The fuel (diesel) supply was realized with a flow regulating pump and a membrane pulsation dampener. Downstream of the pulsation dampener, a check valve, a filter (250 μm pore size), a magnetic valve as well as temperature, and pressure sensors were integrated. The fuel is injected into the mixing chamber through a spray nozzle with a nozzle diameter of 0.2 mm and a spray angle of 60°.

Deionized water was used to supply the fuel mixing chamber with steam necessary for the auto-thermal reforming reaction and to flush the fuel nozzle to avoid coking within the nozzle during heat-up and cool-down procedures. The deionized water is sucked through a filter by a flow controlled pump. Downstream of the pump, the water flows either through an additional filter (250 μm pore size) and a magnetic valve to flush the fuel nozzle or to the steam generator. The steam generator consists of (i) a magnetic valve, (ii) a check valve, (iii) a pressure relief valve, (iv) a vaporizer and superheater, (v) a heated buffer volume, (vi) a pneumatic needle valve, and several temperature and pressure sensors.

For compressed air supply, the central air compressor of the laboratory, where the system is placed, is used. The pressure of the compressed air is reduced to 7 bar absolute and filtered through a three-stage air filter. The compressed air passes manual valves and is used to supply the pneumatic needle valve and air cooling units, e.g. used for the off-gas led to the gas analyzer and flame ionization detector (FID). However, the main part of the compressed air is used to supply the reformer, the SOFC stack, and the catalytic burner. The air mass flow to all of the three mentioned components is controlled by mass flow controllers (MFCs). In addition, several temperature sensors, an air preheating for the reformer and the stack, a magnetic valve to switch the air supply of all MFCs and an additional magnetic valve for the reformer air supply are integrated in the air supply line. The air preheating is done with an electrical heating cartridge.

The fuel mixing and evaporation chamber is one of the critical components of the system and several studies have been conducted in literature to find suitable geometries and operation conditions [25,28,57–59]. The difficulty in the mixing of steam, fuel, and air is especially given if diesel is used as fuel, since the ignition temperature of diesel in air at stoichiometric conditions ($\sim$ 220 °C) is lower than the upper limit of the evaporation range (160 °C–390 °C) [60–62]. Latter can lead to unwanted self-ignition of the mixture upstream of the reformer. Other challenges that can occur are (i) coking of the nozzle, (ii) coking on the mixing chamber walls, and (iii) insufficient fuel evaporation. The fuel mixing chamber in the presented system is an adaption of the final used model in [58]. In this design, steam enters the fuel mixing chamber at a temperature of 400 °C and is led around the fuel nozzle. Air is added tangentially into the mixing chamber downstream of the fuel injection at a temperature of around 300 °C. Although, the temperatures of steam and air in the mixing chamber are above the stated self-ignition temperature of diesel in air, self-ignition was not observed because the self-ignition temperature increases with increasing steam concentrations and decreasing air-fuel ratios [63–65].

The reformer is placed downstream of the fuel mixing unit and consists of a kind of cyclone separation at the inlet to avoid that not evaporated particles are deposited on the catalyst because they could degrade the catalyst as described in [28,60]. The main reactor consists of four parallel tubes, each with a length of 590 mm and an inner diameter of 21 mm. In these tubes, an inert bulk (length of 50 mm), platinum catalysts (0.5 % on 2.7–3.3 mm alumina pellets) (length of 50 mm), and Ni catalysts (length of 490 mm) are placed. Two of the four parallel reforming tubes are equipped with five thermocouples (type N) each. The first thermocouple is placed 67 mm downstream of the inlet and the other thermocouples are placed with a distance of 114 mm between them. Temperatures and pressures are additionally measured at the reformer in- and outlet. The reformer tubes are heated with two separately controllable heating sleeves, one for the inlet half and one for the outlet half of the reformer. The reformer and all parts outside of the SOFC stack furnace are insulated with high temperature resistant fleece (BCTEX).

The SOFC stack is supplied directly with the outlet gas of the reformer and pre-heated compressed air. It is placed inside a furnace. The furnace is also used to heat the reforming gas and air to stack temperature (750 °C). The SOFC stack temperature is monitored at the gas and air in and outlets and four thermocouples (type N) are placed within the stack housing close to the stack at different corners. The stack is electrically connected to an electrical load and impedance analyzer to conduct polarization curve and EIS measurements. The impedance analyzer consists of a signal generator and a data acquisition unit. The EIS is measured with the same method as described in [66]. Between the SOFC stack and the electrical load, a relay is used with

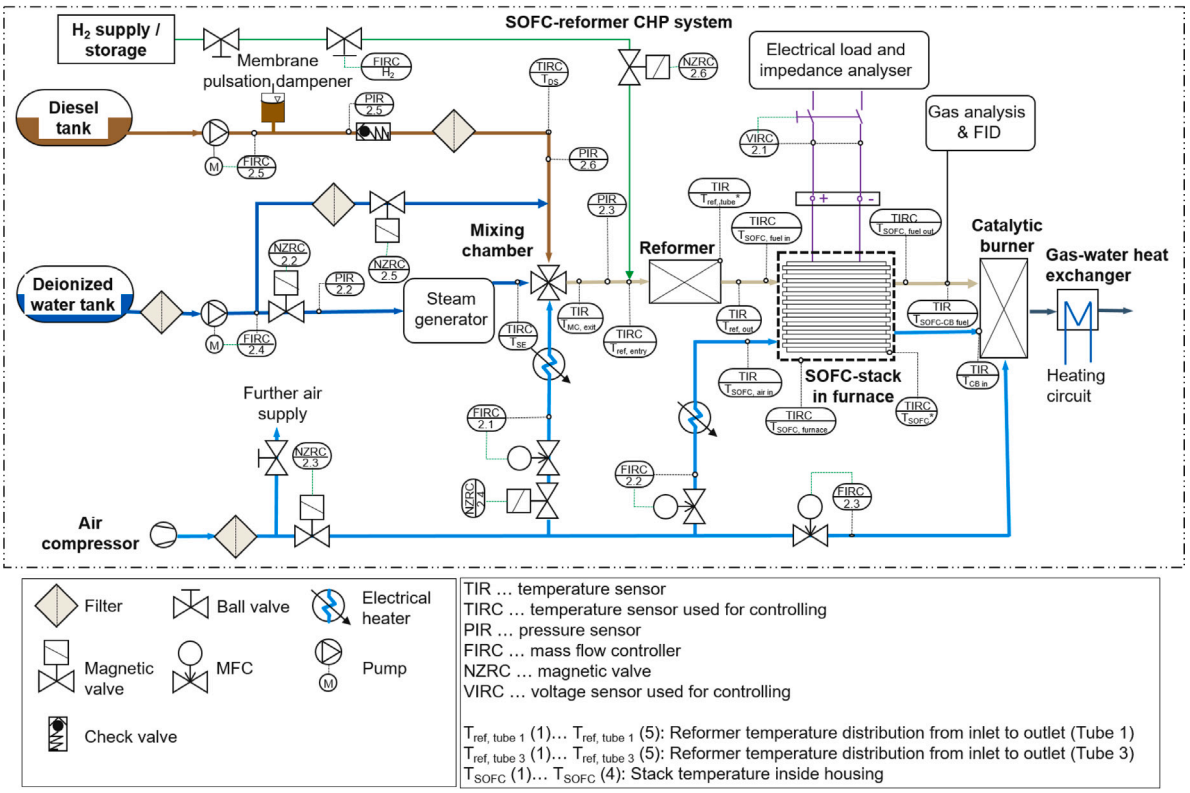

(a)

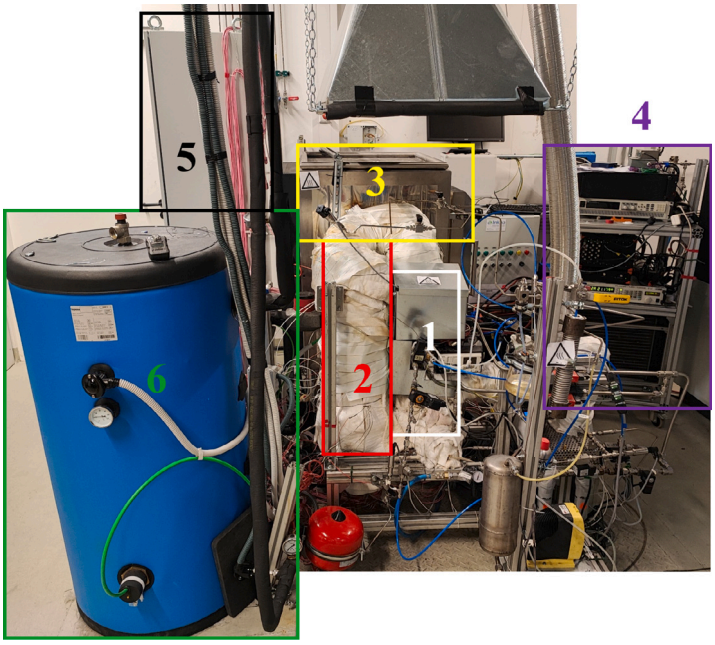

(b)

Fig. 1. (a) P&ID scheme and (b) picture of the developed diesel powered SOFC system.

a separate voltage sensor to disconnect the SOFC stack if the voltage drops below the voltage limit (21 V) for a certain time (500 ms). More information about the SOFC stack can be found in Section 2.2.

The fuel and air off gas of the SOFC stack are led to a catalytic burner, in which platinum catalysts (0.5 % on 2.7–3.3 mm alumina pellets) are placed. In addition to the air stream of the SOFC stack, a cold air stream was added to the catalytic burning unit for cooling purposes. Within the shown tests, the gas analyzer from ABB (modules SCC-C, SCC-F and AO2020) and the FID (FID 2010T-NMHC) from TESTA GmbH are connected to the fuel off gas of the SOFC stack. Since the continuous gas measurements influence the catalytic burner and the heat transferred in the gas-water heat exchanger, these two parts are not further described in this work.

The whole diesel operated SOFC system was controlled by an in house developed control software on a programmable logic controller. The developed control system is able to handle 84 different sensors and

Table 1
Flow rates for presented operating points.

Name –	Diesel in ml(lq) min^{-1}	H_2O in ml(lq) min^{-1}	Air to reformer in slpm	Air to SOFC in slpm	Air to catalytic burner in slpm
OP_{low}	4.41	5.36 (5.36)	13.7	–	–
$OP_{med.\ low}$	6.51	7.91 (8.63)	20.2	–	–
$OP_{med.\ high}$	7.83	9.51 (13.20)	24.3	–	–
OP_{high}	11.64	14.14 (21.45)	36.2	–	–
SR	4.41	14.14	0	55	87
ATR	4.41	14.14	13.7	55	58

actuators, most of the sensors and actuators are shown in Fig. 1(a). The control system further communicates with a greenhouse control system from Inkoa Sistemas S.L., which is able to control heaters and artificial lightning of a greenhouse.

2.2. SOFC stack

The 30 cell SOFC stack integrated and tested in the diesel operated SOFC system was bought from Ningbo SOFCMAN Energy Technology Co. Ltd. (SOFCMAN-SCS2000). The stack was delivered in a self-compressed configuration. It has a nominal output power of 2 kW and consists of 30 single anode supported cells. Each cell has an active cell area of around 144 cm^2 and consists of a Ni-YSZ (yttria-stabilized zirconia) anode, a YSZ electrolyte, a LSCF (lanthanum strontium cobalt ferrite) - GDC (gadolinium doped ceria) cathode, and a GDC interlayer between the cathode and the electrolyte. The interconnectors and end plates of the stack consist of SUS430 stainless steel. The stack is operated in cross-flow configuration and has an open air outlet, which made it necessary to develop a separate stack housing to collect the outlet air flow and led it to the catalytic burner. The fuel gas inlet and outlet, as well as the air inlet are integrated in the stack design and can be accessed via tubes welded on one end plate.

2.3. Testing conditions

The diesel operated SOFC system was tested in several steps and the diesel reforming tests and the final system tests are presented in this work. The preliminary diesel reforming tests were conducted with four different operating points, which all have the same steam to carbon ratio ($H_2O/C = 1.13$) and oxygen to carbon ratio ($O_2/C = 0.49$), see Table 1. However, during the initial diesel reforming tests, a local hot spot was discovered at the inlet of the reformer, which led to self-ignition of the gas mixture upstream of the reformer. As a solution to this problem, the steam flow rate is automatically adapted to control the reformer inlet temperature. Latter led to increased steam flow rates for operating points $OP_{med.\ low}$- OP_{high}, see values in parenthesis in Table 1. To definitely avoid changing steam amounts during SOFC operation to gain reasonable EIS measurements, the operating points were adapted and the operating points SR and ATR from Table 1 are used to test the whole system. These points are a mixture of OP_{low} and the steam flow rate of OP_{high}.

The operating points were checked for theoretical carbon formation and Ni re-oxidation by calculating the limits for carbon formation and Ni re-oxidation and drawing the limits and operating points in a C-H-O ternary diagram, see Fig. 2. To draw the fuel compositions in the ternary diagram, the fuel is analyzed for its composition of C (85.32 weight%), H (13.94 weight%), O (0.62 weight%), *N* (0.11 weight%), and S (5.9 mg/kg) at the Institute of Chemistry at the University of Graz. The previously discussed increase of the steam flow rate for $OP_{med.\ low}$ to OP_{high} in Table 1 changes these compositions towards H_2O, see Fig. 2 (OP_{low}-OP_{high} increased H_2O).

Previous to the conducted tests presented in this paper, the diesel operated reformer or the SOFC system are prepared according to the following steps: (i) mechanical and thermal cleaning or replacing of soiled tubes, (ii) tightness tests of the tubing (iii) inserting new commercial available catalysts and the commercial available SOFC according to the description in Section 2.1, (iv) calibration and/or testing of all used sensors (temperature, pressure, voltage, current), pumps, flow controllers and measurement devices (gas analyzer and FID), and (v) checking the spray pattern, pressure loss, and fuel flow through the fuel nozzle. All chemical active parts (catalysts and the SOFC stack) are replaced before the presented tests and are commercially available. The volume of the bulks in the reformer are specified in Section 2.1, leading to minimization of subjective influence on the test preparation.

3. Results and discussion

The results section of this work is divided into preliminary diesel reforming tests and the proof of concept of the system operation. The preliminary diesel reforming tests were conducted before the reforming unit was connected to the other parts of the developed system. This is done to avoid fast and severe system degradation due to possible insufficient reforming of the fuel mixture caused by control errors or not optimized operating conditions.

3.1. Preliminary reforming tests

Within this section, the diesel reforming tests, which were conducted before the system tests, are presented and discussed. To monitor the diesel reforming process, the temperature profiles and the dry reformer off-gas composition are continuously measured. The reformer off-gas composition was further compared with chemical equilibrium calculations for the tested gas composition and reforming temperature. The diesel reforming tests were done using the same system as presented in Fig. 1(a), except that the reformer off-gas was directly cooled down and led to the gas analyzer, the FID and in the exhaust gas ventilation.

The temperature profile is measured along two of four reformer tubes continuously during the diesel reforming experiments. The temporal average temperature profile of these tubes is shown in Fig. 3(a)–3(d). In addition, the mean temperature of the reformer tubes (tube 1: $T_{ref,\ tube\ 1}(1)$ - $T_{ref,\ tube\ 1}(5)$, tube 3: $T_{ref,\ tube\ 3}(1)$ - $T_{ref,\ tube\ 3}(5)$) over time is shown in Figs. 3(e) and 3(f). The reformer inlet temperature upstream of the reformer ($T_{ref,\ entry}$) is controlled to not exceed 700 °C by adjusting the steam flow rate. As shown in Figs. 3(a) and 3(b), the average temperature at the reformer inlet is below the set maximum of 700 °C for all tested gas compositions. The two heating sleeves around the reformer tubes are controlled by $T_{ref,\ tube\ 1}(2)$ and $T_{ref,\ tube\ 1}(5)$, respectively, and the target temperature is set to 800 °C. A local hot spot is observed in tube 1 at $T_{ref,\ tube\ 1}(4)$, see Fig. 3(a). By comparing the temperature at this location during the tests, with the temperature measured before operation with diesel (operation with hydrogen and steam), see Fig. 3(c), it seems that the local hot spot originates from non-ideal located heating sleeves and is not influenced by other processes. To ensure that no other processes are responsible for the hot spot, the relative temperature distribution is used. The relative temperature ΔT_i distributions in the tubes 1 and 3, Figs. 3(c) and 3(d), respectively, is calculated by subtracting the temporal average temperature at the measurement position i of steam and hydrogen operation $T_{i,mean}(H_2,\ H_2O)$ from the temporal average temperature at

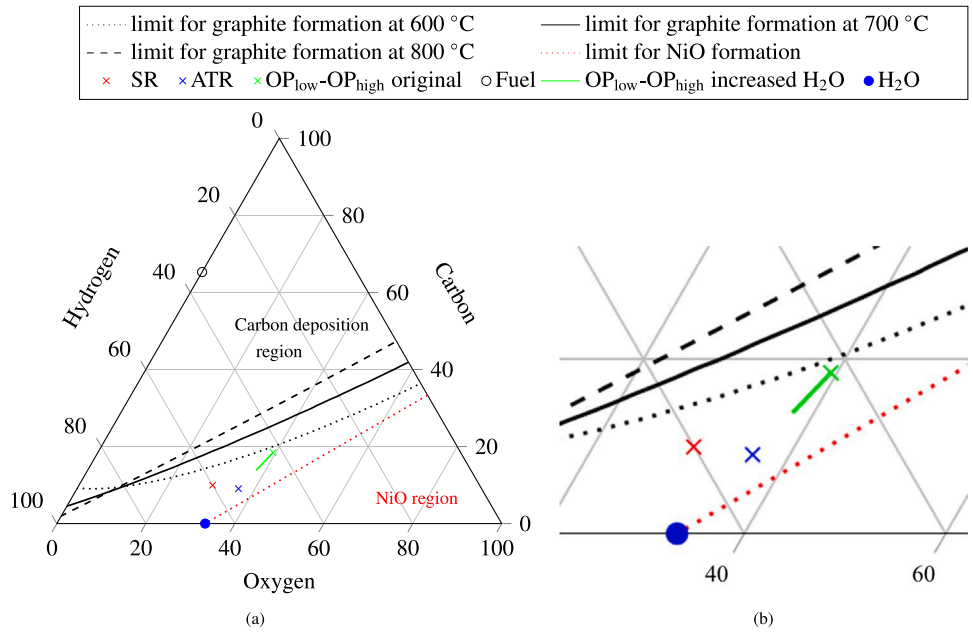

Fig. 2. (a) Calculated C-H-O ternary diagram and (b) detail view of the area where the tested gas compositions are located.

the measurement position i of the individual operating points (OP_{low} - OP_{high}) $T_{i,mean}$(diesel reforming), see Eq. (1).

$$\Delta T_i = \frac{\sum_{j=1}^{n} T_{i,j}(\text{diesel reforming})}{n} - \frac{\sum_{k=1}^{m} T_{i,k}(H_2,\ H_2O)}{m} = T_{i,mean}(\text{diesel reforming}) - T_{i,mean}(H_2,\ H_2O) \quad (1)$$

Hence, mainly temperature changes caused by chemical reactions are visible in Figs. 3(c) and 3(d). The temporal average temperature in Eq. (1) is calculated as the sum of measurement values during the specific time intervals (e.g. $\sum_{j=1}^{n} T_{i,j}$(diesel reforming)) divided by the number of measurement values in the specific time interval (n, m). The relative temperature distribution shows no big differences between the tubes, which leads to the conclusion that the reforming reactions are also similar in both tubes. Hence, the flow rate through both tubes should be similar. However, three reaction zones along the reforming reactor can be identified. The first one from $T_{ref,\ entry}$ to $T_{ref,\ tube\ 1}(1)/T_{ref,\ tube\ 3}(1)$ (tube 1/tube 3) is dominated by the exothermal partial oxidation reaction, visible in high relative temperatures and rising absolute temperatures. Within the partial oxidation reaction zone, higher total volume flows lead to higher temperatures, which is related to the higher ratio of generated heat to heat losses. The second reaction zone reaches from $T_{ref,\ tube\ 1}(1)/T_{ref,\ tube\ 3}(1)$ to $T_{ref,\ tube\ 1}(4)/T_{ref,\ tube\ 3}(4)$. Within this zone, temperatures below the temperature of hydrogen and steam operation are observed. Latter leads to the conclusion that the endothermic steam reforming reaction is dominant in this section. Within the third section, $T_{ref,\ tube\ 1}(4)/T_{ref,\ tube\ 3}(4)$ to $T_{ref,\ out}$, the absolute temperature decreases, but the relative temperature rises. Hence, this section might be influenced by the water gas shift reaction and the additional heating.

The results of the gas analysis and FID measurements of the preliminary diesel reforming tests are shown in Fig. 4. They are compared with the calculated chemical equilibrium gas composition at the temporal average mean temperature of the reformer. The chemical equilibrium of the fuel mixture is calculated with the diesel fuel modeled as a mixture of $C_{11}H_{10}$ (0.2 mol%) and $C_{16}H_{34}$ (0.8 mol%). This modeled fuel composition has the same H/C ratio as the analyzed fuel and it is used for all calculations within this work. The chemical equilibrium calculations in this work are done with the software HSC Chemistry. The sum of hydrocarbons for the calculated equilibrium composition consists of more than 99.9999% of methane but other hydrocarbons

Table 2
Calculated flow rates from gas analysis measurements presented in Fig. 4.

Name –	H_2 in slpm	CO in slpm	CO_2 in slpm	N_2 in slpm
OP_{low}	8.4	3.9	2.1	10.8
$OP_{med.\ low}$	10.9	5.4	3.0	16.0
$OP_{med.\ high}$	11.9	5.8	3.4	19.2
OP_{high}	18.6	9.7	4.7	28.6

such as C_2H_6 and C_2H_4 are also taken into account for the chemical equilibrium calculations. Moreover, the possibility for solid carbon formation is also considered in the equilibrium calculations. The gas analysis and FID results are temporal average values and the shown error bars are the standard deviations of the temporal averages. Across all tested operating points, a good agreement between the measured and equilibrium gas composition was observed. The sum of hydrocarbons including methane, is measured with the FID and was below 200 ppm(vol) for OP_{low} to $OP_{med.\ high}$. Only OP_{high} showed a higher hydrocarbon slip with more than 600 ppm(vol). The calculated flow rates of the dry reformer off gases based on the mass balance of the reformer and the measured dry gas composition are shown in Table 2. Within these experiments OP_{high} reached approximately 2.3 times the flow rate of CO and H_2 of OP_{low}, which is equivalent to a partial load of around 43% for OP_{low} if OP_{high} is defined as full load case.

Differences visible between the measured and equilibrium gas composition for $OP_{med.\ low}$ to OP_{high} in Fig. 4 seem to be explainable by insufficient water-gas shift reaction. The higher percentage of H_2 in OP_{low} could be caused by slight pressure fluctuations in the fuel supply, which could lead to changed fuel flow rates.

3.2. System operation

In this section, the system operation with diesel is investigated with focus laid on fuel reforming and SOFC characterization during short term tests. The section is split into three parts. In the first part, the fuel reforming process is investigated, the second part is about the characterization of the SOFC, and the last part is about the SOFC efficiency and utilization rates.

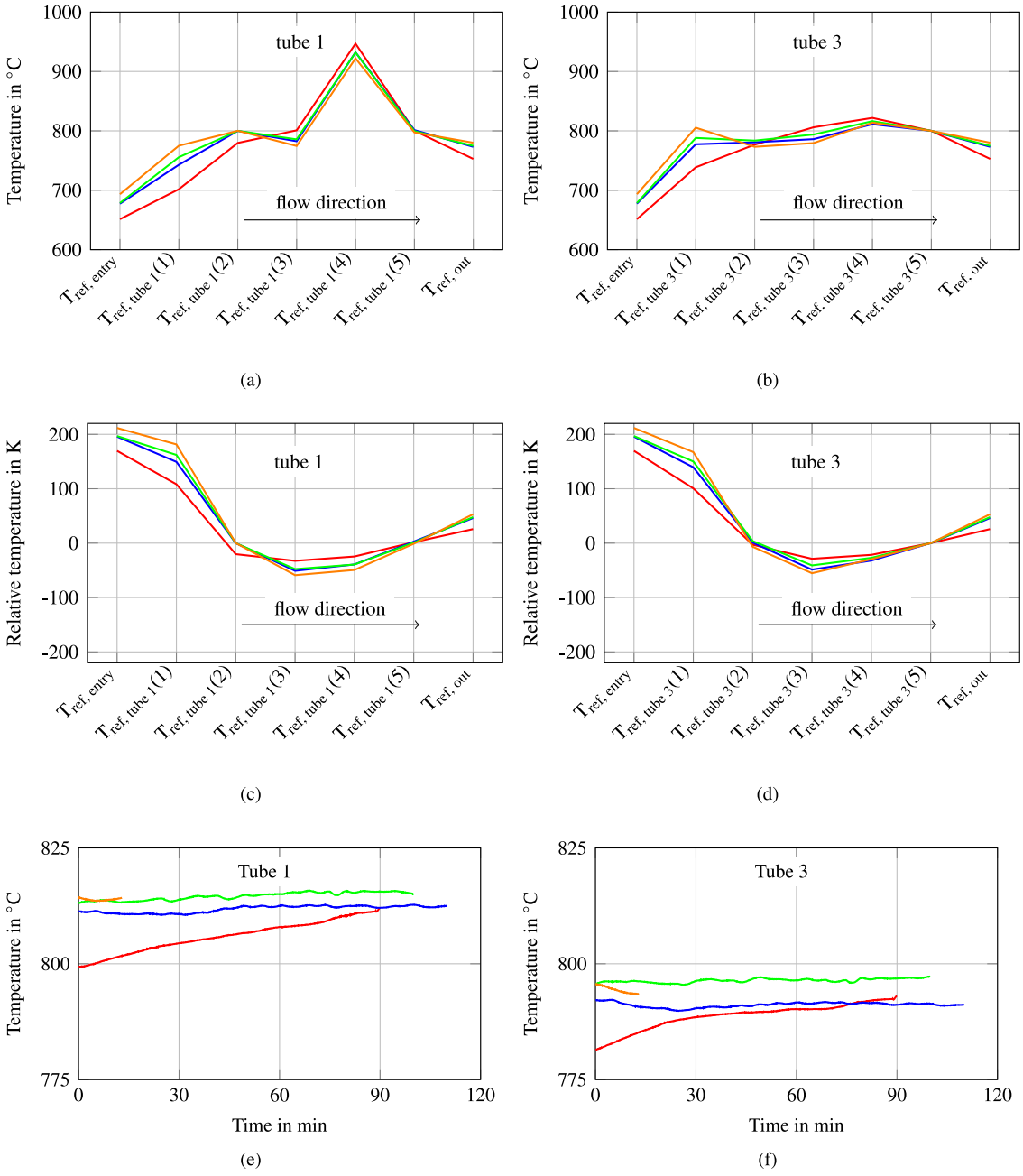

Fig. 3. Average temperature distribution along the reformer: (a) absolute temperature of tube 1, (b) absolute temperature of tube 3. (c) Relative temperature of tube 1, (d) relative temperature of tube 3. Mean reformer temperature over time for (e) tube 1 and (f) tube 3 for — OP_{low}, — $OP_{med.\ low}$, — $OP_{med.\ high}$, — OP_{high}.

3.2.1. Reforming

In this section, the diesel reforming process during the SOFC system test is investigated. Here, the temperature distribution along the reformer for the different operating points and the mean reformer temperatures over time are presented in the same style as in Section 3.1.

The temporal average absolute temperature distribution of reformer tube 1 and 3 are shown in Figs. 5(a) and 5(b), respectively. The local hot spot, which was present in the preliminary diesel reforming tests, see Fig. 3, was avoided by rearranging the heating sleeves. The control temperature had to be reduced for the system tests from initial 800 °C (as in the preliminary tests) to 780 °C due to internal shorts of the heating sleeves at higher temperatures. In contrast to the operating points applied for the preliminary diesel reforming test, not only auto-thermal reforming compositions were used, but one auto-thermal composition was compared with one steam reforming composition. The investigated steam reforming composition is always used as an intermediate step during the automated heat up procedure. As shown in Fig. 5, the control temperature of 780 °C is not reached at $T_{ref,\ tube\ 1}(2)$, only for $T_{ref,\ tube\ 1}(5)$, since approximately 854 W would be needed to reach equilibrium conditions at 780 °C for steam reforming and heating sleeves with 2 × 700 W are installed along the reformer. The heat input is evenly distributed along the reformer, which leads to lower temperatures at the reformer inlet and approximately the control temperature at the reformer outlet. The relative temperature distribution (reforming temperature distribution minus temperature distribution with H_2/H_2O operation) reveals a decreasing temperature from $T_{ref,\ tube\ 1}(1)/T_{ref,\ tube\ 3}(1)$ to $T_{ref,\ tube\ 1}(3)/T_{ref,\ tube\ 3}(3)$ and downstream of $T_{ref,\ tube\ 1}(3)/T_{ref,\ tube\ 3}(3)$, the temperature rises again, see Figs. 5(c) and 5(d). The rise in relative temperature is explained by increasing amount of added heat, a decreasing influence of the steam reforming reaction and the exothermal water gas shift reaction. The

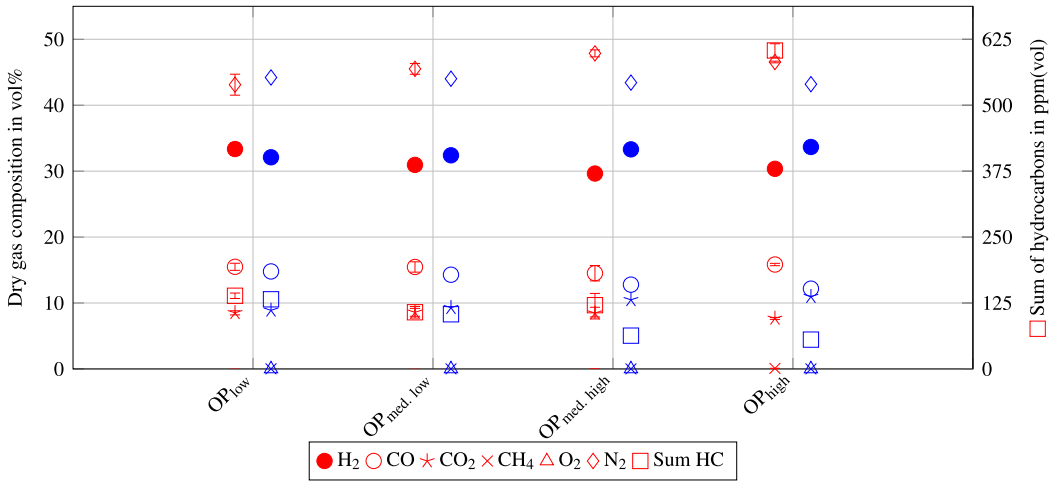

Fig. 4. • Measured (mean and standard deviation) and • calculated chemical equilibrium dry gas composition downstream of the reformer.

relative temperature decrease at the reformer inlet seems to be mainly caused by an insufficient heating and locally concentrated endothermal diesel steam reforming reactions. During auto-thermal reforming conditions, the temperature distribution along the reformer shows values close to the control temperature of 780 °C for both control elements ($T_{ref,\ tube\ 1}(2)$ and $T_{ref,\ tube\ 1}(5)$), see Figs. 5(a) and 5(b). The reformer inlet temperature ($T_{ref,\ entry}$) is cooler as it was for the preliminary tests with the same diesel and air flow rates. This is likely the case because of the increased steam flow which reduces the impact of the partial oxidation reaction. However, it is still visible, especially in the relative temperature distribution, that the partial oxidation reaction is taking place around $T_{ref,\ tube\ 1}(1)/T_{ref,\ tube\ 3}(1)$, where the platinum catalyst is placed. The endothermal steam reforming reaction seems to be dominant between $T_{ref,\ tube\ 1}(1)/T_{ref,\ tube\ 3}(1)$ and $T_{ref,\ tube\ 1}(3)/T_{ref,\ tube\ 3}(3)$. Downstream of $T_{ref,\ tube\ 1}(3)/T_{ref,\ tube\ 3}(3)$, the additional heating and water gas shift reaction is visible. The same reaction zones and similar relative temperature distributions observed for the preliminary diesel reforming tests and the system test indicate a reproducible reforming process.

The dynamic behavior of the diesel reformer during the system test is visible in the mean reformer temperature over time, see Figs. 5(e) and 5(f). Both steam and auto-thermal diesel reforming showed a stable temperature after 40 min of operation. Even so, auto-thermal reforming starting from the cooler steam reforming temperature distribution, while steam reforming is switched on after H_2 and H_2O operation. Still, the average reformer temperature had clearly less fluctuations for auto-thermal reforming compared to steam reforming.

3.2.2. SOFC characterization

In this section, the behavior of the SOFC stack operated with steam and auto-thermally reformed diesel is investigated. For this purpose, the SOFC off-gas is continuously analyzed with a gas analyzer and FID, polarization curves are measured, electrochemical impedance spectroscopy is conducted, and the advanced tool of distribution of relaxation times is applied.

The temporal average gas analysis of points where the current was held constant is shown in Fig. 6. In Figs. 6(a) and 6(b), the dry gas composition of the steam reforming operation is shown for the increasing current ramp and decreasing current ramp, respectively. During the current increase, Fig. 6(a), the measured dry gas composition downstream of the SOFC stack is close to the equilibrium composition at the control temperature of the SOFC stack of 750 °C. While decreasing the current step by step, a bigger deviation between the measured gas composition and equilibrium composition is visible above 200 mA cm^{-2}. This deviation could be caused by a fuel flow variation indicated by a fluctuation of the fuel nozzle pressure which is observed in the respective time range. Continued reduction of the current density lead to a further approach of the measured gas composition and the equilibrium composition. The gas analysis after a SOFC button cell operated with auto-thermally reformed liquid hydrocarbons presented by Siefert et al. [49] also shows a gas composition close to the calculated chemical equilibrium.

The gas analysis of the auto-thermal gas composition is shown in Figs. 6(c) and 6(d) for an increasing and decreasing current ramp, respectively. The measured gas compositions shows lower percentages of H_2 and CO_2, but higher percentages of CO and N_2. This suggests that parts of the deviation can be explained by an incomplete water gas shift reaction. Another possibility is the not completed reforming of hydrocarbons. However, the sum of hydrocarbons measured during auto-thermal reforming is beneath 200 ppm(vol) for all applied electrical currents. Comparing auto-thermal reforming to steam reforming while decreasing the current (Fig. 6(d) compared to 6(b)), no similar deviations as in Fig. 6(b) are found and also no fluctuations of the fuel nozzle pressure are observed. Hence, the more stable operation during auto-thermal reforming, which was observed in Section 3.2.1, is also present in the gas analysis downstream of the SOFC.

The polarization curve of the SOFC stack is measured according to the gas analysis data during ramping the current of the SOFC stack up and down. Due to possible local temperature deviations within the 30 cell stack, potential micro-structural changes of the cells at the highest current densities and possible slight fluctuations in the fuel supply, the curves are not fitting perfectly and are shown for all four cases (ATR and SR during ramping current up and down) in Figs. 6(e) and 6(f). The temperature deviation of the SOFC (mean of $T_{SOFC,\ fuel\ in}$, $T_{SOFC}(2)$, and $T_{SOFC,\ fuel\ out}$) during measuring the polarization curves stayed within 9 K for all measurements except for ramping down the current under SR conditions. There the lowest temperature, which is measured at the lowest current, is 22 K below the highest temperature, which is measured at the highest current. It should also be mentioned here that the stack is implemented in a diesel operated system and several system components can influence the stack voltage. In Fig. 6(e), only the raw, continuous measured parts of the polarization curves are shown and, in Fig. 6(f), only the mean values of the current steps and the standard deviation of the voltages at these steps are shown. For steam reforming, the current is increased up to 347 mA cm^{-2}. At this point, a pressure fluctuation in the diesel nozzle likely resulted in a reduction in fuel flow rate, which was already observed in Fig. 6. The fuel fluctuation likely caused a voltage decrease from initially nearly 24 V (SR current up) to less than 22 V (SR current down), see Fig. 6(e). The voltage degradation vanished while holding the SOFC stack at 208 mA cm^{-2} during decreasing the current and from there on, the polarization curves are nearly identical.

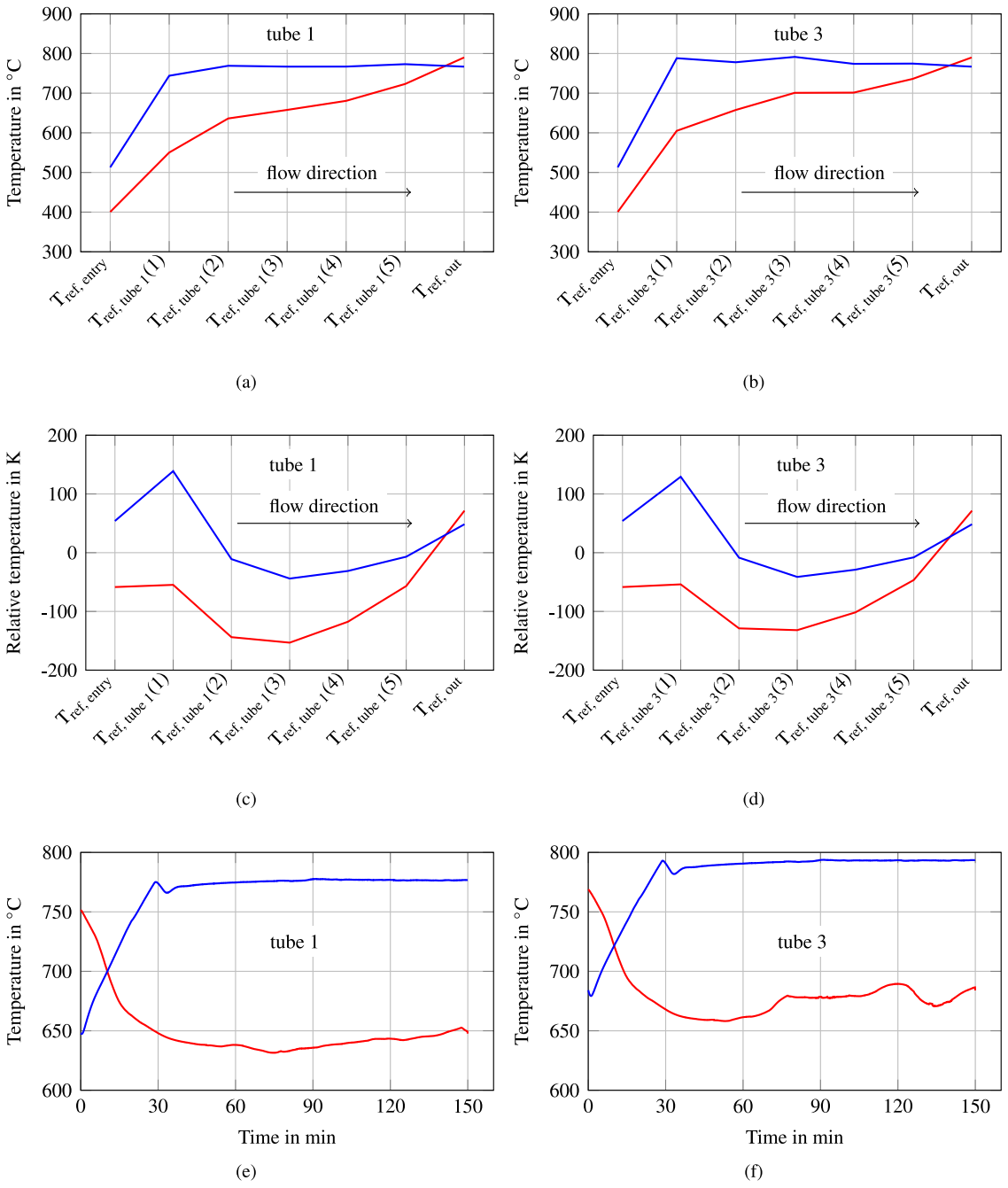

Fig. 5. Average temperature distribution along the reformer: (a) absolute temperature of tube 1, (b) absolute temperature of tube 3. (c) Relative temperature of tube 1, (d) relative temperature of tube 3. Mean reformer temperature over time for (e) tube 1 and (f) tube 3 for — SR and — ATR.

During operation with the auto-thermal gas composition, the SOFC stack was loaded up to 243 mA cm^{-2}. At 243 mA cm^{-2}, the voltage decreased from initially 22 V (ATR current up) to 21 V (ATR current down) and stayed at this level, see Fig. 6(e). Non ideal gas distribution in the 30 cell stack and the low stack voltage could have led to some individual cell voltages dropping below the limit of 0.7 V, which could have caused this change in voltage. No direct operational reasons are found in the sensor data of the system, but the voltage drop will be discussed in more detail in the following EIS and DRT evaluation.

The electrochemical impedance spectra of the stack are measured at different current levels while ramping the current down. For ATR operating conditions, EIS measurements are conducted at 208.3 mA cm^{-2} before increasing the current to 243 mA cm^{-2} (ATR 01 208.3 mA cm^{-2}) and after decreasing the current from 243 mA cm^{-2} (ATR 02 208.3 mA cm^{-2}). In Figs. 7(a) and 7(b), the raw data of the measured impedance spectra which passes the Kramers–Kronigtest with less than 5% deviation are shown. The data presented lies in the frequency range between 0.5 Hz to 1 kHz. In addition to the raw measurement data, the back-calculated impedance data from the DRT spectra are shown to qualitatively verify the agreement of the measurement data and the DRT fit. A good agreement between the raw measurement data and the back-calculation from the DRT spectra is shown for all curves even so the same DRT parameter are used for all spectra to make them comparable. Only the measured impedance for ATR at 99 mA cm^{-2} shows kind of a discontinuity in the low frequency arc, see Fig. 7(b). For this case, the low frequency peak (P_{LF}) of the DRT spectrum has to be interpreted carefully. It has to be considered, that other system components could also influence the EIS measurements.

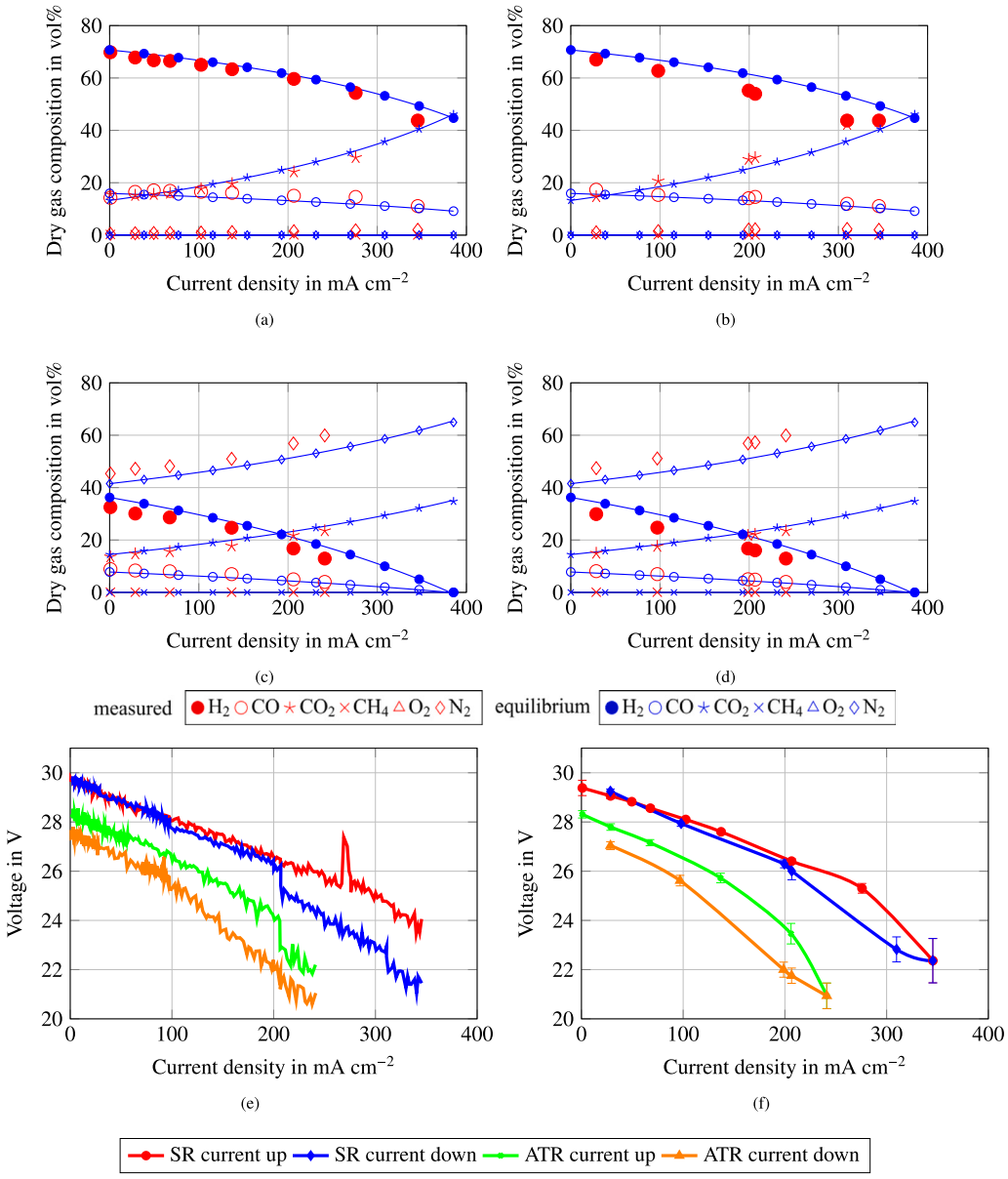

Fig. 6. Measured dry gas composition and calculated chemical equilibrium dry gas composition over current density for (a) SR current ramp up, (b) SR current ramp down, (c) ATR current ramp up, (d) ATR current ramp down downstream of the SOFC stack, and polarization curves measured for (e) continuously changing currents and (f) mean voltage with standard deviation for steady currents.

The EIS curves measured during SR operation, see Fig. 7(a), show similar ohmic resistances, between 0.79 Ω cm^2 and 0.85 Ω cm^2 for the current densities between 312.5 mA cm^{-2} and 201.4 mA cm^{-2}. The ohmic resistance of SR at 99 mA cm^{-2} is 0.96 Ω cm^2, which is slightly higher compared to measurements at other current densities. Latter could be caused by local temperature decreases within the SOFC stack. However, the change in ohmic resistance does not seem to be the main influencing factor for the changing cell performance observed in the polarization curves in Figs. 6(e) and 6(f) for operation with SR. Otherwise, SR at 312.5 mA cm^{-2} would show the highest ohmic resistance because the highest voltage deviation between ramping the current up and down is observed at this current density. Compared to operation with SR, operation with ATR shows in total higher and more changing ohmic resistances, see Fig. 7(b). The lowest ohmic resistance is observed for ATR 01 at 208.3 mA cm^{-2} (1.06 Ω cm^2), which is measured while ramping the current up. The highest ohmic resistance is observed for ATR 02 at 208.3 mA cm^{-2} (1.66 Ω cm^2), which is measured while ramping the current down from 243.1 mA cm^{-2}. The different ohmic resistances at the same current density before and after drawing a current of 243.1 mA cm^{-2} seems to be one cause of the voltage drop observed in the polarization curves in Figs. 6(e) and 6(f). The following measurements at 201.4 mA cm^{-2} and at 99 mA cm^{-2} at ATR conditions show a reduction of the ohmic resistance towards the initial resistance of the measurement ATR 01 at 208.3 mA cm^{-2}, see Fig. 7(b). This trend is also observed in the polarization curve measurements shown in Figs. 6(e) and 6(f), where the deviation of the polarization curves decreases towards lower current densities.

The polarization resistance of the EIS spectra is visible in Figs. 7(c) and 7(d) for operation with SR and ATR, respectively. In these figures, the polarization resistance of the back-calculated EIS spectra from DRT are visible. Due to too noisy signals below 0.5 Hz, a direct interpretation of measurement data has to be done with care, but due to the good fit of the DRT back-calculation, see Figs. 7(a) and 7(b), it seems as the same trends are visible for measurement and back-calculation. For operation with SR, the polarization resistance seems to be dependent on the current density or fuel utilization, as also observed in [67]. A

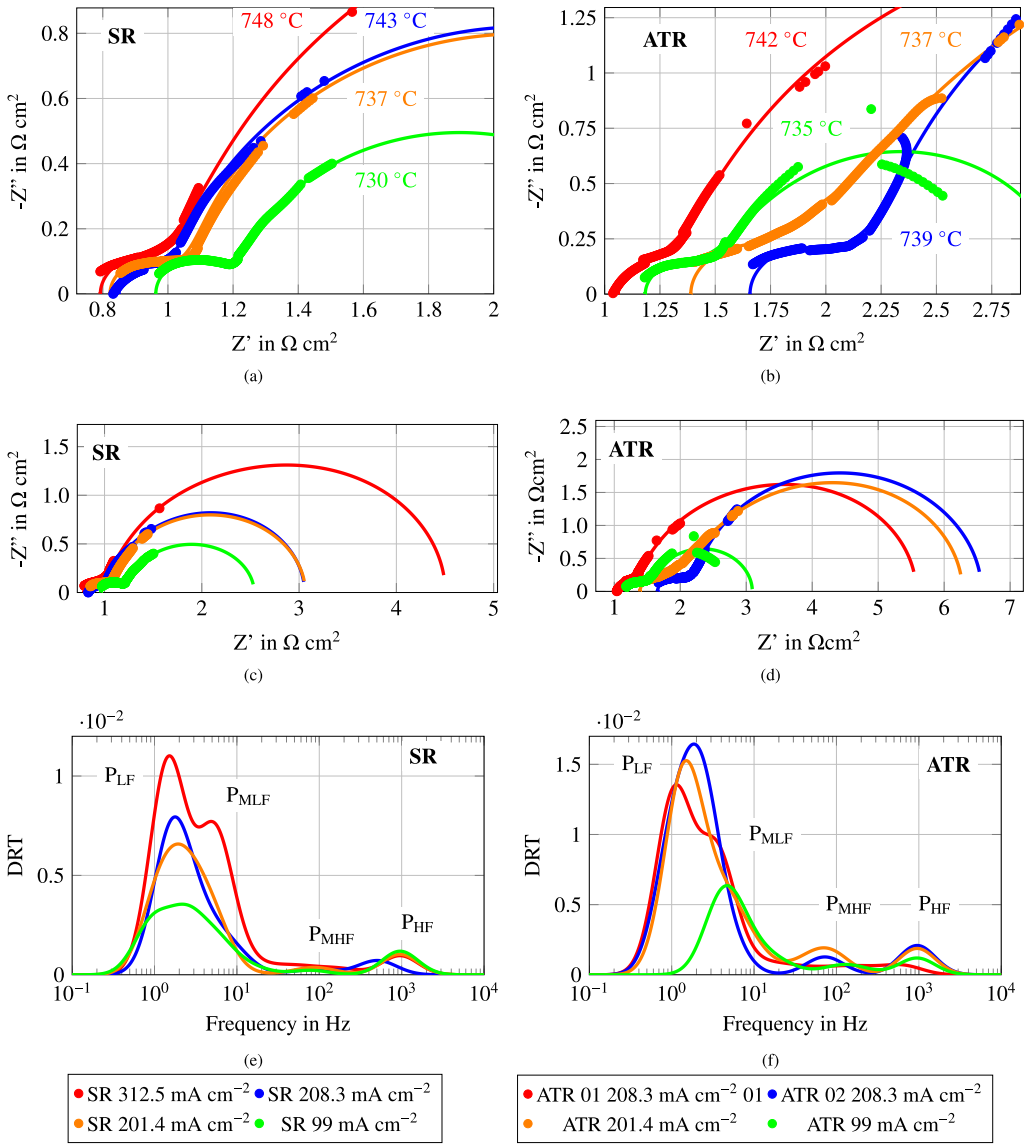

Fig. 7. (a) and (b) show a zoom on the measurement data and the mean temperature of the SOFC stack along the EIS measurement (c) and (d) show the whole area of the Nyquist plots of (°) measured EIS and (–) from DRT back-calculated EIS. (e) and (f) show the DRT spectra. (a), (c), and (e) refer to operating at SR conditions, (b), (d), and (f) refer to operating at ATR conditions.

dependency of the polarization resistance on the current density is also visible for operation with ATR. In addition, the polarization resistance increased from ATR 01 at 208.3 mA cm^{-2} (4.48 Ω cm^2) to ATR 02 at 208.3 mA cm^{-2} (4.88 Ω cm^2). Overall, the Nyquist plots reveal higher losses for operation with ATR compared to operation with SR, which results in the reduced power output observed in Figs. 6(e) and 6(f).

For a more detailed evaluation of the EIS data, the DRT tool is applied and the resulting DRT spectra are presented in Figs. 7(e) and 7(f) for operation with SR and ATR, respectively. Three peaks, a low frequency peak (P_{LF}), a medium high frequency peak (P_{MHF}), and a high frequency peak (P_{HF}), are mainly visible for the DRT spectra in the observed frequency range with a fourth peak (P_{MLF}) in the medium low frequency range merging with P_{LF}. All three observed peaks are higher under ATR conditions compared to SR conditions, resulting in higher losses under ATR conditions, which is consistent with the Nyquist plots and polarization curves investigated previously. For interpretation of DRT spectra, literature data and additional information of operating conditions are necessary. However, since no EIS measurements or DRT analysis for diesel operated SOFC stack systems are available in the literature, to the best of the authors knowledge, other comparable studies and additional applied measurement methods are used for the interpretation of the DRT spectra. In the DRT spectra for SR operation, Fig. 7(e), the low frequency peaks seem to be mainly influenced by the current density. The increasing current density causes (i) increasing product concentration [68,69], (ii) increasing losses due to gas diffusion and conversion in the fuel electrode substrate [38,68,70,71], and (iii) increasing losses due to O_2 diffusion and surface exchange processes in the air electrode [70,72,73]. All of the mentioned losses are observed at a frequency range between 10^0 Hz and 10^1 Hz, the same range where P_{LF} is located. The same effects also apply to P_{LF} at ATR conditions in Fig. 7(f). The observed increase of P_{LF} in Fig. 7(f) from ATR 01 at 208.3 mA cm^{-2} to ATR 02 at 208.3 mA cm^{-2} might be caused by operation at low voltages and high current densities, as described in the discussion of the polarization curves in Figs. 6(e) and 6(f). These operating conditions could have led to local fuel starvation which can cause re-oxidation of the Ni based fuel electrode. Re-oxidation of the

fuel electrode during operation of a cell with reformed diesel is also observed in [37]. The re-oxidation would explain the increase in ohmic resistance due to worse conductivity of NiO compared to Ni and the larger volume of NiO hinders gas diffusion processes, leading to an increase of the polarization resistance and P_{LF}.

The medium low frequency peaks P_{MLF}, which are not clearly separated from P_{LF}, are located around 5 Hz and follow the same trend as P_{LF} for SR conditions. However, the DRT spectrum of ATR at 99 mA cm^{-2} shows only a medium low frequency peak without a low frequency peak. This seems to be the case due to the discontinuity in the measured EIS spectrum. Nevertheless, ATR at 99 mA cm^{-2} in Fig. 7(f) follows the overall same trend for decreasing losses as SR at 99 mA cm^{-2} in Fig. 7(e).

The medium high frequency peaks P_{MHF} are located between 50 Hz and 200 Hz and, according to literature it could be influenced by (i) a changing steam partial pressure at the fuel electrode [68,69], (ii) O_2 diffusion and surface exchange processes at the air electrode [70,72,73], and (iii) O_2 surface exchange kinetics and O^{2-} diffusivity in the air electrode bulk [38]. P_{MHF} shows higher amplitudes only for ATR 02 at 208.3 mA cm^{-2} and ATR at 201.4 mA cm^{-2}. However, the high frequency peaks P_{HF} are higher compared to P_{MHF} and are located at around 10^3 Hz. Possible influences of P_{HF} are, according to literature, (i) charge transfer and ionic conduction processes in the fuel electrode [70,73,74], (ii) SOFC temperature [69], (iii) gas diffusion coupled with charge transfer and ionic transport in the fuel electrode [38], and (iv) electron transfer between the air electrode and the current collector [72]. Laying the focus on SR operation, Fig. 7(f), only SR at 208.3 mA cm^{-2} is shifted towards lower frequencies. Since the air side is operated constant, a temporary change in gas diffusion coupled with charge transfer and ionic conduction processes in the fuel electrode is likely. The polarization curves in Figs. 6(e) and 6(f) also show a voltage change at 208.3 mA cm^{-2}. In contrast, P_{HF} for ATR conditions shows a clear trend. The smallest high frequency peak is observed for ATR 01 at 208.3 mA cm^{-2} and ATR 02 at 208.3 mA cm^{-2} holds the highest high frequency peak. The trend is the same as for P_{LF}. Hence, it is likely that gas diffusion coupled with charge transfer and ionic conduction processes in the fuel electrode are the main influence of the change. This can again be explained by a local fuel starvation leading to re-oxidation of the Ni based fuel electrode caused during operation at high current densities.

3.2.3. Efficiency and utilization

In the following, the system efficiency and power output of the developed diesel operated SOFC system is investigated. The focus is laid on efficiency of SOFC operation and fuel utilization, as the system design is aimed at research friendliness rather than heat loss reduction or heat recuperation.

There are several definitions of efficiencies for SOFCs, such as the reversible thermodynamic efficiency, the voltage efficiency, the effective electrical cell efficiency, and the cell efficiency considering fuel utilization, which is a combination of the reversible thermodynamic efficiency and the voltage efficiency [75,76]. The effective electrical efficiency of a SOFC is defined as the electrical power output divided by the energy input from the fuel. In Eq. (2), the effective electrical efficiency is defined as the power output of the SOFC (voltage times current output of the SOFC = $U_{SOFC}\ I_{SOFC}$) divided by the lower fuel heating value per mass fuel (LHV_{Fuel}) times the fuel mass flow ($\dot{m}_{Fuel}$). Depending on literature, also the higher fuel heating value per mass fuel could be used instead of LHV_{Fuel}, which leads to lower efficiencies:

$$\eta_{el.,SOFC} = \frac{\text{useful energy output}}{\text{energy input}} = \frac{U_{SOFC}\ I_{SOFC}}{LHV_{Fuel}\ \dot{m}_{Fuel}} \tag{2}$$

The effective electrical efficiency of the SOFC for the SOFC system tests is shown in Fig. 8(a). There, the initial diesel supply is defined as the input fuel. The curve of the effective electrical efficiency in Fig. 8(a) can also be used to show the electrical power output of the SOFC stack, since the same constant fuel input is used for SR and ATR conditions. The maximum measured power outputs are $1,112 \pm 43$ W at 347 mA cm^{-2} for SR, and 727 ± 16 W at 243.1 mA cm^{-2} for ATR conditions. Steam reforming seems to be beneficial for the effective electrical efficiency compared to auto-thermal reforming, since the additional external heat demand for the steam reforming process is not included in Eq. (2). However, peak values of around $42.5 \pm 1.6\%$ at 347 mA cm^{-2} for steam reforming conditions and $27.8 \pm 0.6\%$ at 243.1 mA cm^{-2} for auto-thermal reforming conditions were reached. In Fig. 8(b), the energy input from the fuel is defined as the chemically bound energy in the gas composition downstream of the reformer. The gas composition downstream of the reformer is defined as the chemical equilibrium composition. Hence, the partial oxidation of fuel in the reformer during ATR operation is not directly visible in Fig. 8(b) in contrast to Fig. 8(a). This leads to similar effective electrical efficiencies for ATR ($35.1 \pm 0.8\%$) and SR ($35.9 \pm 1.4\%$). The effective electrical efficiency for SR is lower in 8(b) compared to 8(a) because the heating value of the fuel is increased during the steam reforming process. However, the main influence on the effective electrical efficiency in Figs. 8(a) and 8(b) is the fuel slip through the stack since SOFCs are not capable of utilizing 100% of the fuel. The fuel utilization rate gives information about the amount of fuel, that is converted to electrical energy compared to the amount of fuel that enters the system or the SOFC, see Eq. (3).

$$\begin{aligned} U_{fuel,SOFC} &= \frac{\text{fuel oxidized}}{\text{fuel available}} = \frac{\dot{m}_{Fuel,\ oxidized}}{\dot{m}_{Fuel}} \\ &= \frac{\text{oxygen conducted through the electrolyte}}{\text{oxygen flow to stoichiometrically oxidize the fuel}} = \\ &= \frac{I_{SOFC}}{z\ F\ \dot{n}_{Fuel}\ \sum_j (\nu_{j,stoichiometric\ O}\ \nu_j)} \\ &= \frac{I_{SOFC}}{z\ F\ \dot{n}_{Fuel}\ (27\ \nu_{C_{11}H_{10}} + 49\ \nu_{C_{16}H_{34}})} \end{aligned} \tag{3}$$

In Eq. (3), z is the number of moles electrons transferred per mole elemental oxygen, which is 2 since SOFCs are conducting O^{2-} ions. F is the Faraday constant, $\dot{n}_{Fuel}$ is the total molar fuel flow rate, $\nu_{j,stoichiometric\ O}$ is the amount of elemental oxygen required for the stoichiometric oxidation of one mole of species j, and ν_j is the molar fraction of species j in the fuel. An example for a fuel mixture of $C_{11}H_{10}$ and $C_{16}H_{34}$ is shown in Eq. (3). The oxygen utilization rate is defined analogue to the fuel utilization, see Eq. (4). Here, $\dot{n}_{Air,\ SOFC}$ is the molar flow rate of air supplied to the SOFC air electrode and ν_{O_2} is the molar fraction of O_2 in air.

$$\begin{aligned} U_{oxy,SOFC} &= \frac{\text{oxygen conducted through the electrolyte}}{\text{oxygen available}} = \\ &= \frac{I_{SOFC}}{z\ F\ \dot{n}_{Air,\ SOFC}\ (2\ \nu_{O_2})} \end{aligned} \tag{4}$$

Both the fuel and oxygen utilization are shown in Fig. 8(c) for only diesel as fuel input along the current density. Since the diesel flow rate and the air flow rate for the SOFC air electrode are the same for SR and ATR operation, the utilization rates per current density are also the same for both operating conditions. The fuel and oxygen utilization within the SOFC using the equilibrium gas composition at the reformer outlet as fuel input are shown in Fig. 8(d). The oxygen utilization is not changed compared to Fig. 8(c), but the partial oxidation within the reformer during ATR operation is considered in the fuel utilization rate. The fuel utilization rate within the reformer at ATR conditions is 33%. This results in 63% fuel utilization within the SOFC ($U_{fuel,SOFC,ref,out}$) at a current density of 243.1 mA cm^{-2} for ATR conditions, compared to 60% at SR conditions at a current density of 347 mA cm^{-2}. Fig. 8 shows that the effective electrical efficiency ($\eta_{el.,SOFC}$) depends on the definition of input fuel and fuel utilization rates in the SOFC-stack. Due to the constant fuel input and the dependency of the effective electrical efficiency on the fuel utilization rate, an increase of the effective electrical efficiency is observed for increasing current in Figs. 8(a) and 8(b). To minimize the influence of the fuel utilization rate on

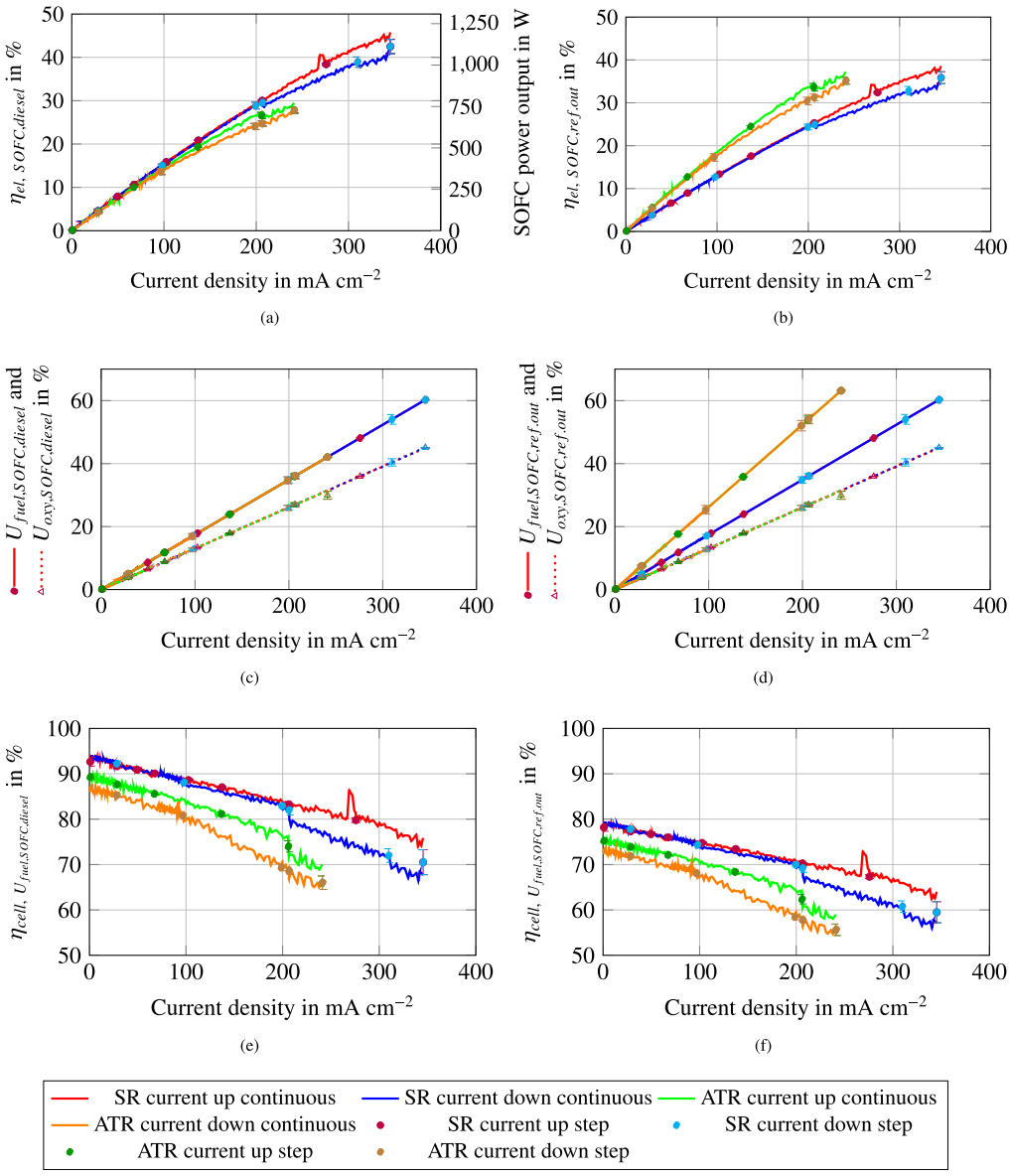

Fig. 8. (a) Effective electrical efficiency related to diesel as fuel input and power output. (b) Effective electrical efficiency related to chemical equilibrium at 750 °C as fuel input. (c) Oxygen and fuel utilization of the SOFC related to diesel as fuel input. (d) Oxygen and fuel utilization of the SOFC related to chemical equilibrium at 750 °C as fuel input. (e) SOFC cell efficiency considering fuel utilization related to diesel as fuel input. (e) SOFC cell efficiency considering fuel utilization related to chemical equilibrium at 750 °C as fuel input. For (-) continuous current change and (•) current steps.

the effective electrical efficiency, an anode off-gas recirculation can be used. Anode off-gas recirculation for diesel operated SOFC systems is demonstrated in [52,77] and the possible effective electrical efficiency gain is shown in [78]. If the fuel gas slip through the SOFC is not taken into account due to possible recirculation or other usage of the fuel slip stream, the SOFC efficiency can be defined as cell efficiency considering fuel utilization ($\eta_{cell,\,U_{fuel,SOFC}}$). The cell efficiency considering fuel utilization compares the electrical output power of the SOFC with the heating value from the fuel oxidized in the SOFC, see Eq. (5).

$$\eta_{cell,\,U_{fuel,SOFC}} = \frac{U_{SOFC}\,I_{SOFC}}{LHV_{Fuel}\,\dot{m}_{Fuel,\,oxidized}} = \frac{\eta_{el.,SOFC}}{U_{fuel,SOFC}} \tag{5}$$

Here, $\dot{m}_{Fuel,\,oxidized}$ is equal to the amount of fuel oxidized within the cell. The cell efficiency considering fuel utilization is shown in Figs. 8(e) and 8(f). In Fig. 8(e), diesel is defined as fuel. In this way, the effective electrical efficiency from Fig. 8(a) divided by the fuel utilization in Fig. 8(c) is equal to cell efficiency considering fuel utilization in Fig. 8(e). The cell efficiency considering fuel utilization shows the same trend as the polarization curve since the cell efficiency considering fuel utilization is equal to the measured voltage divided by the potential derived from the lower heating value. The cell efficiency considering fuel utilization has its highest values at lowest current densities because it represents the, in our case, constant losses from the reversible thermodynamic efficiency plus the losses of irreversible kinetic effects in the fuel cell (voltage efficiency) [75]. The cell efficiency considering fuel utilization is the maximum reachable electrical system efficiency for the applied SOFC operating conditions and fuel cell. The effective electrical cell efficiency approaches the cell efficiency considering fuel utilization for increasing fuel utilization. Hence, it would be beneficial to operate the fuel cell at low current densities and high fuel utilization.

The same also applies to the cell efficiency considering fuel utilization shown in Fig. 8(f). There, the equilibrium gas composition at the reformer outlet is defined as fuel input. Due to the increase of the lower heating value of the fuel during the reforming process, the cell efficiency considering fuel utilization shown in Fig. 8(f) is lower than the cell efficiency considering fuel utilization shown in Fig. 8(e).

Summarizing this part, we presented four different electrical efficiencies for each operating condition of the SOFC (SR and ATR) depending on the definition of the efficiency itself and the fuel input. Depending on what should be compared or to show possible potentials, different efficiency definitions should be used. A common efficiency definition, especially for auxiliary power units, might be the net electrical efficiency which compares the useable electrical energy output minus the electrical energy input with the absolute fuel input [53,56,79]. However, since such systems are more or less complex and a variety of losses can occur, the net electrical efficiency cannot give any information about the source of losses or potential efficiencies of SOFC driven power generators with complex fuels which can differ for even slightly different system designs. In our study we found that, depending on the current density the potential maximum electrical efficiency ($\eta_{cell,\ U_{fuel,SOFC,diesel}}$) is above 65% for diesel as fuel with higher efficiencies at partial load conditions.

4. Conclusion and outlook

Within this work, we presented the system design and testing of an in house developed diesel operated combined heat and power SOFC system. The approach of our system design is research friendly, but with an applicable power output. In addition, detailed monitoring of the system should be possible to investigate electrochemical impedance spectroscopy and distribution of relaxation time results for future application of these measurements in liquid hydrocarbon driven SOFC systems. For this purpose, the diesel reforming unit was tested with different diesel flow rates and monitored via measurement of the temperature distribution along the catalyst. The SOFC stack was characterized with EIS, DRT, and polarization curve measurements for diesel steam reforming and diesel auto-thermal reforming conditions. In addition, continuous gas analysis was applied to monitor the off-gas of the reformer or the SOFC. To identify the potential of SOFC application with liquid hydrocarbons, different efficiency definitions for the SOFC were calculated and discussed for the two operating points (diesel steam and diesel auto-thermal reforming) tested.

We found gas compositions downstream the diesel reformer to be close to chemical equilibrium conditions with less than 650 ppm(vol) hydrocarbon slip. The reformer outlet flow rate of H_2 and CO was varied with the factor of 2.3 of the lowest inlet flow rate showing a good load flexibility. During SOFC operation, a local Ni re-oxidation seemed to occur during high fuel utilization rates and a low stack voltage. The performance change and degradation mechanism was identified by successful application of EIS measurements and their evaluation with the DRT tool. The efficiency analysis of the SOFC showed that around 42.5% of the lower heating value of the diesel input were converted in electrical energy at fuel utilization rates of 60%, resulting in 70% cell efficiency considering fuel utilization.

The results shown within this work contribute directly to the knowledge basis for EIS and DRT results, which is necessary for their interpretation and understanding. The demonstration of EIS measurements and DRT analysis of a 30 cell SOFC stack in a diesel operated SOFC system is done for the first time, to the best of the authors knowledge. Although the EIS measurement might be influenced from several system components, a high data quality is obtained, allowing detailed interpretation of the measurement results and Laying the foundation for future application of EIS and DRT measurements as advanced online monitoring tools even of complex SOFC systems. In addition, monitoring and controlling of the entire system including several balance of plant components was achieved. The existent system should in future be used to study long term behavior of different components and applicability of other liquid fuels such as bio-diesel and methanol. On this basis, the design concept could be shifted from research friendliness to more efficient system operation. In addition, the interaction of the system in an already built heating and energy supply system, e.g. a greenhouse, could be tested.

The following abbreviations are used in this manuscript:

APU	Auxiliary power unit
DRT	Distribution of relaxation time
EIS	Electrochemical impedance spectroscopy
FID	Flame ionization detector
GDC	Gadolinium doped ceria
H_2O/C	Steam to carbon ratio
LSCF	Lanthanum strontium cobalt ferrite
MFC	Mass flow controller
O_2/C	Oxygen to carbon ratio
P_{HF}	High frequency peak
P_{LF}	Low frequency peak
P_{MHF}	Medium high frequency peak
P_{MLF}	Medium low frequency peak
POx	Partial oxidation
P&ID	Piping and Instrumentation Diagram
slpm	Standard litre per minute
SOFC	Solid oxide fuel cell
SOE	Solid oxide electrolyzer
WGS	Water gas shift
YSZ	Yttria stabilized zirconia
Z	Impedance

CRediT authorship contribution statement

Michael Höber: Conceptualization, Methodology, Software, Formal analysis, Investigation, Resources, Data curation, Writing – original draft, Writing – review & editing, Visualization, Project administration. **Benjamin Königshofer:** Conceptualization, Software, Investigation, Resources. **Pavle Boškoski:** Investigation, Resources, Data curation. **Christoph Hochenauer:** Funding acquisition. **Vanja Subotić:** Conceptualization, Methodology, Resources, Writing – review & editing, Supervision, Project administration, Funding acquisition.

Declaration of competing interest

The authors declare that they have no known competing financial interests or personal relationships that could have appeared to influence the work reported in this paper.

Data availability

Data will be made available on request.

Acknowledgments

This project has been funded by partners of the ERA-Net SES 2018 joint call RegSys (www.eranet-smartenergysystems.eu) - a network of 30 national and regional RTD funding agencies of 23 European countries. As such, this project has received funding from the European Union's Horizon 2020 research and innovation program under grant agreement no. 775970. The authors gratefully acknowledge the funding of this project entitled "AGRO-SOFC" (Grant No. 872299) by The Austrian Research Promotion Agency (FFG). We also want to mention that this work is done within the research initiative "Sustainable People- and Goods Transportation".

References

[1] A. Lachuriya, R.D. Kulkarni, Stationary electrical energy storage technology for global energy sustainability: A review, in: 2017 International Conference on Nascent Technologies in Engineering, (ICNTE), IEEE, 2017, pp. 1–6, http://dx.doi.org/10.1109/ICNTE.2017.7947936, URL http://ieeexplore.ieee.org/document/7947936/.

[2] C. Chen, F. Jiao, B. Lu, T. Liu, Q. Liu, H. Jin, Challenges and perspectives for solar fuel production from water/carbon dioxide with thermochemical cycles, Carbon Neutrality 2 (1) (2023) 9, http://dx.doi.org/10.1007/s43979-023-00048-6, http://creativecommons.org/licenses/by/4.0/.CarbonNeutrality, https://link.springer.com/10.1007/s43979-023-00048-6.

[3] W. Zhang, Y. Li, L. Wang, F. Zhang, Y. Ai, G. Shao, P. Zhang, In situ construction of cyano-modified g-c3n4 nanolayer-coated srtio3 nanotubes by gas-solid reaction for efficient photocatalytic solar fuel production, Chem. Eng. J. 469 (2023) 143817, http://dx.doi.org/10.1016/j.cej.2023.143817, URL https://linkinghub.elsevier.com/retrieve/pii/S1385894723025482.

[4] G. Falciani, E. Chiavazzo, An overview on modelling approaches for photochemical and photoelectrochemical solar fuels processes and technologies, Energy Convers. Manage. 292 (2023) 117366, http://dx.doi.org/10.1016/j.enconman.2023.117366, URL https://linkinghub.elsevier.com/retrieve/pii/S0196890423007124.

[5] Y. Zhao, Z. Niu, J. Zhao, L. Xue, X. Fu, J. Long, Recent advancements in photoelectrochemical water splitting for hydrogen production, Electrochem. Energy Rev. 6 (1) (2023) 14, http://dx.doi.org/10.1007/s41918-022-00153-7, URL https://link.springer.com/10.1007/s41918-022-00153-7.

[6] G. Cinti, A. Baldinelli, A. Di Michele, U. Desideri, Integration of solid oxide electrolyzer and Fischer-Tropsch: A sustainable pathway for synthetic fuel, Appl. Energy 162 (2016) 308–320, http://dx.doi.org/10.1016/j.apenergy.2015.10.053, URL https://linkinghub.elsevier.com/retrieve/pii/S0306261915012805.

[7] S. Siccardi, J. Amici, S. Colombi, J.T. Carvalho, D. Versaci, E. Quartarone, L. Pereira, F. Bella, C. Francia, S. Bodoardo, UV-cured self-healing gel polymer electrolyte toward safer room temperature lithium metal batteries, Electrochim. Acta 433 (2022) 141265, http://dx.doi.org/10.1016/j.electacta.2022.141265, URL https://linkinghub.elsevier.com/retrieve/pii/S0013468622014220.

[8] L. Fagiolari, D. Versaci, F. Di Berardino, J. Amici, C. Francia, S. Bodoardo, F. Bella, An exploratory study of MoS2 as anode material for potassium batteries, Batteries 8 (11) (2022) 242, http://dx.doi.org/10.3390/batteries8110242, https://www.mdpi.com/2313-0105/8/11/242/htm, https://www.mdpi.com/2313-0105/8/11/242.

[9] Z. Huang, P. Jaumaux, B. Sun, X. Guo, D. Zhou, D. Shanmukaraj, M. Armand, T. Rojo, G. Wang, High-energy room-temperature sodium–sulfur and sodium–selenium batteries for sustainable energy storage, Electrochem. Energy Rev. 6 (1) (2023) 21, http://dx.doi.org/10.1007/s41918-023-00182-w, URL https://link.springer.com/10.1007/s41918-023-00182-w.

[10] C. Ding, Z. Chen, C. Cao, Y. Liu, Y. Gao, Advances in Mn-based electrode materials for aqueous sodium-ion batteries, Nano-Micro Lett. 15 (1) (2023) 192, http://dx.doi.org/10.1007/s40820-023-01162-x, URL https://link.springer.com/10.1007/s40820-023-01162-x.

[11] L. Wang, W.J.-Y. Ke, R.-X. Wu, M. Tripathy, H. Mokhlis, K.H. Chua, A.V. Prokhorov, T.H. Nguyen, M.M. Farid, A. Subiantoro, K. Li, B. Chong, S. Azizi, A.A. Jahromi, D. Xu, Stability evaluation of a grid-tied hybrid wind/PV farm joined with a hybrid energy-storage system, Sustain. Environ. Res. 33 (1) (2023) 21, http://dx.doi.org/10.1186/s42834-023-00181-y, URL https://sustainenvironres.biomedcentral.com/articles/10.1186/s42834-023-00181-y.

[12] A.M. Hussain, E.D. Wachsman, Liquids-to-power using low-temperature solid oxide fuel cells, Energy Technol. 7 (1) (2019) 20–32, http://dx.doi.org/10.1002/ente.201800408, URL https://onlinelibrary.wiley.com/doi/10.1002/ente.201800408.

[13] M.A. Abdelkareem, W.H. Tanveer, E.T. Sayed, M.E.H. Assad, A. Allagui, S. Cha, On the technical challenges affecting the performance of direct internal reforming biogas solid oxide fuel cells, Renew. Sustain. Energy Rev. 101 (2019) 361–375, http://dx.doi.org/10.1016/j.rser.2018.10.025, URL https://linkinghub.elsevier.com/retrieve/pii/S1364032118307287.

[14] P. Nehter, B. Wildrath, A. Bauschulte, K. Leites, Diesel based SOFC demonstrator for maritime applications, ECS Trans. 78 (1) (2017) 171–180, http://dx.doi.org/10.1149/07801.0171ecst, URL https://iopscience.iop.org/article/10.1149/07801.0171ecst.

[15] M. Santarelli, M. Cabrera, M. Calí, Solid oxide fuel based auxiliary power unit for regional jets: Design and mission simulation with different cell geometries, J. Fuel Cell Sci. Technol. 7 (2) (2010) 0210061–02100611, http://dx.doi.org/10.1115/1.3176282.

[16] K. DePippo, B.A. Peppley, Canadian remote community power generation: How reformer and fuel cell systems compare with diesel generators, Int. J. Energy Res. 43 (3) (2019) 1161–1170, http://dx.doi.org/10.1002/er.4345, URL http://doi.wiley.com/10.1002/er.4345.

[17] L. Barelli, G. Bidini, G. Cinti, Operation of a solid oxide fuel cell based power system with ammonia as a fuel: Experimental test and system design, Energies 13 (23) (2020) 6173, http://dx.doi.org/10.3390/en13236173, URL https://www.mdpi.com/1996-1073/13/23/6173.

[18] A. Weber, Fuel flexibility of solid oxide fuel cells, Fuel Cells (2021) http://dx.doi.org/10.1002/fuce.202100037, fuce.202100037, URL https://onlinelibrary.wiley.com/doi/10.1002/fuce.202100037.

[19] B. Stoeckl, M. Preininger, V. Subotić, S. Megel, C. Folgner, C. Hochenauer, Towards a wastewater energy recovery system: The utilization of humidified ammonia by a solid oxide fuel cell stack, J. Power Sources 450 (2020) 227608, http://dx.doi.org/10.1016/j.jpowsour.2019.227608, https://linkinghub.elsevier.com/retrieve/pii/S0378775319316015.

[20] H. Zhu, R.J. Kee, Thermodynamics of SOFC efficiency and fuel utilization as functions of fuel mixtures and operating conditions, J. Power Sources 161 (2) (2006) 957–964, http://dx.doi.org/10.1016/J.JPOWSOUR.2006.05.006.

[21] M. Lo Faro, S. Trocino, S. Zignani, C. Italiano, A. Vita, A. Aricò, Study of a solid oxide fuel cell fed with n-dodecane reformate. Part II: Effect of the reformate composition, Int. J. Hydrogen Energy 42 (3) (2017) 1751–1757, http://dx.doi.org/10.1016/j.ijhydene.2016.06.048, URL https://linkinghub.elsevier.com/retrieve/pii/S0360319916311156.

[22] A. Lindermeir, S. Kah, S. Kavurucu, M. Mühlner, On-board diesel fuel processing for an SOFC–APU—Technical challenges for catalysis and reactor design, Appl. Catal. B 70 (1–4) (2007) 488–497, http://dx.doi.org/10.1016/j.apcatb.2006.02.025, URL https://linkinghub.elsevier.com/retrieve/pii/S0926337306002074.

[23] J. Pasel, J. Meisner, Z. Pors, R. Samsun, A. Tschauder, R. Peters, Autothermal reforming of commercial jet A-1 on a 5kWe scale, Int. J. Hydrogen Energy 32 (18) (2007) 4847–4858, http://dx.doi.org/10.1016/j.ijhydene.2007.07.060, URL https://linkinghub.elsevier.com/retrieve/pii/S0360319907004302.

[24] N. Li, B. Liu, L. Jia, D. Yan, J. Li, Liquid biofuels for solid oxide fuel cells: A review, J. Power Sources 556 (2023) 232437, http://dx.doi.org/10.1016/j.jpowsour.2022.232437, URL https://linkinghub.elsevier.com/retrieve/pii/S0378775322014148.

[25] S. Martin, G. Kraaij, T. Ascher, P. Baltzopoulou, G. Karagiannakis, D. Wails, A. Wörner, Direct steam reforming of diesel and diesel–biodiesel blends for distributed hydrogen generation, Int. J. Hydrogen Energy 40 (1) (2015) 75–84, http://dx.doi.org/10.1016/j.ijhydene.2014.10.062, URL https://linkinghub.elsevier.com/retrieve/pii/S0360319914029024.

[26] J. Boon, E. van Dijk, S. de Munck, R. van den Brink, Steam reforming of commercial ultra-low sulphur diesel, J. Power Sources 196 (14) (2011) 5928–5935, http://dx.doi.org/10.1016/j.jpowsour.2011.03.009, URL https://linkinghub.elsevier.com/retrieve/pii/S0378775311005283.

[27] H.A.J. Van Dijk, J.P. Ouweltjes, R.G. Nyqvist, Diesel CPO for SOFC development of a cold-flame assisted CPO reactor coupled to a SOFC, in: Energy Research Centre of the Netherlands, 2009, p. 38, URL https://publications.tno.nl/publication/34628957/9mEZ26/e09031.pdf.

[28] J. Bae, S. Lee, S. Kim, J. Oh, S. Choi, M. Bae, I. Kang, S.P. Katikaneni, Liquid fuel processing for hydrogen production: A review, Int. J. Hydrogen Energy 41 (44) (2016) 19990–20022, http://dx.doi.org/10.1016/j.ijhydene.2016.08.135, URL https://linkinghub.elsevier.com/retrieve/pii/S0360319916325228.

[29] P. Nehter, J.B.g. Hansen, P.K. Larsen, A techno-economic comparison of fuel processors utilizing diesel for solid oxide fuel cell auxiliary power units, J. Power Sources (2011) http://dx.doi.org/10.1016/j.jpowsour.2010.09.011.

[30] J. Pasel, R.C. Samsun, R. Peters, B. Thiele, D. Stolten, Long-term stability at fuel processing of diesel and kerosene, Int. J. Hydrog. Energy 39 (31) (2014) 18027–18036, http://dx.doi.org/10.1016/j.ijhydene.2014.03.148, URL www.sciencedirect.com.

[31] J. Pasel, R. Samsun, A. Tschauder, R. Peters, D. Stolten, A novel reactor type for autothermal reforming of diesel fuel and kerosene, Appl. Energy 150 (2015) 176–184, http://dx.doi.org/10.1016/j.apenergy.2015.04.038.

[32] J. Pasel, R.C. Samsun, J. Meißner, A. Tschauder, R. Peters, Recent advances in diesel autothermal reformer design, Int. J. Hydrogen Energy 45 (3) (2020) 2279–2288, http://dx.doi.org/10.1016/j.ijhydene.2019.11.137, URL https://linkinghub.elsevier.com/retrieve/pii/S0360319919343599.

[33] D. Potemkin, V. Rogozhnikov, N. Ruban, V. Shilov, P. Simonov, M. Shashkov, V. Sobyanin, P. Snytnikov, Comparative study of gasoline, diesel and biodiesel autothermal reforming over Rh-based FeCrAl-supported composite catalyst, Int. J. Hydrogen Energy 45 (49) (2020) 26197–26205, http://dx.doi.org/10.1016/j.ijhydene.2020.01.076, URL https://linkinghub.elsevier.com/retrieve/pii/S0360319920302214.

[34] R.C. Samsun, M. Prawitz, A. Tschauder, J. Meißner, J. Pasel, R. Peters, Reforming of diesel and jet fuel for fuel cells on a systems level: Steady-state and transient operation, Appl. Energy 279 (2020) 115882, http://dx.doi.org/10.1016/j.apenergy.2020.115882, URL https://linkinghub.elsevier.com/retrieve/pii/S0306261920313532.

[35] T.A. Wierzbicki, I.C. Lee, A.K. Gupta, Recent advances in catalytic oxidation and reformation of jet fuels, Appl. Energy 165 (2016) 904–918, http://dx.doi.org/10.1016/j.apenergy.2015.12.057, URL https://linkinghub.elsevier.com/retrieve/pii/S030626191501630X.

[36] I. Kang, Y. Kang, S. Yoon, G. Bae, J. Bae, The operating characteristics of solid oxide fuel cells driven by diesel autothermal reformate, Int. J. Hydrogen Energy 33 (21) (2008) 6298–6307, http://dx.doi.org/10.1016/j.ijhydene.2008.07.123, https://www.sciencedirect.com/science/article/pii/S0360319908008306, https://linkinghub.elsevier.com/retrieve/pii/S0360319908008306.

[37] J. Jeong, S.-W. Baek, J. Bae, A diesel-driven, metal-based solid oxide fuel cell, J. Power Sources 250 (2014) 98–104, http://dx.doi.org/10.1016/j.jpowsour.2013.10.100, URL https://linkinghub.elsevier.com/retrieve/pii/S0378775313017667.

[38] A. Kromp, S. Dierickx, A. Leonide, A. Weber, E. Ivers-Tiffée, Electrochemical analysis of sulfur-poisoning in anode supported SOFCs fuelled with a model reformate, J. Electrochem. Soc. 159 (5) (2012) B597–B601, http://dx.doi.org/10.1149/2.015206jes, URL https://iopscience.iop.org/article/10.1149/2.015206jes.

[39] J. Kupecki, D. Papurello, A. Lanzini, Y. Naumovich, K. Motylinski, M. Blesznowski, M. Santarelli, Numerical model of planar anode supported solid oxide fuel cell fed with fuel containing H2S operated in direct internal reforming mode (DIR-SOFC), Appl. Energy 230 (2018) 1573–1584, http://dx.doi.org/10.1016/j.apenergy.2018.09.092, URL https://linkinghub.elsevier.com/retrieve/pii/S030626191831403X.

[40] Y. Kikuchi, J. Matsuda, Y. Tachikawa, Y. Shiratori, S. Taniguchi, K. Sasaki, Degradation of SOFCs by various impurities: Impedance spectroscopy and microstructural analysis, ECS Trans. 78 (1) (2017) 1253–1260, http://dx.doi.org/10.1149/07801.1253ecst.

[41] C.-K. Lin, T.-T. Chen, A.-S. Chen, Y.-P. Chyou, L.-K. Chiang, Finite element analysis of thermal stress distribution in planar SOFC, ECS Trans. 7 (1) (2007) 1977–1986, http://dx.doi.org/10.1149/1.2729310, https://iopscience.iop.org/article/10.1149/1.2729310, https://iopscience.iop.org/article/10.1149/1.2729310/meta.

[42] M. Höber, B. Königshofer, P. Wachter, G. Nusev, P. Boskoski, C. Hochenauer, V. Subotić, Holistic approach to design, test, and optimize stand-alone sofc-reformer systems, Processes 9 (2) (2021) 1–28, http://dx.doi.org/10.3390/pr9020348, URL https://www.mdpi.com/2227-9717/9/2/348.

[43] V. Subotić, C. Hochenauer, Analysis of solid oxide fuel and electrolysis cells operated in a real-system environment: State-of-the-health diagnostic, failure modes, degradation mitigation and performance regeneration, Prog. Energy Combust. Sci. 93 (2022) 101011, http://dx.doi.org/10.1016/J.PECS.2022.101011.

[44] M. Höber, P. Wachter, B. Königshofer, F. Mütter, H. Schröttner, C. Hochenauer, V. Subotić, In operando electrochemical impedance spectroscopy monitoring of nickel catalysts for hydrogen production, part I: Methodology and performance characterization, Fuel 324 (2022) 124256, http://dx.doi.org/10.1016/j.fuel.2022.124256, URL https://linkinghub.elsevier.com/retrieve/pii/S001623612201105X.

[45] N. Müller, R. Moos, A. Jess, In situ monitoring of coke deposits during coking and regeneration of solid catalysts by electrical impedance-based sensors, Chem. Eng. Technol. 33 (1) (2010) 103–112, http://dx.doi.org/10.1002/ceat.200900380.

[46] D. Rauch, P. Fremerey, A. Jess, R. Moos, In situ detection of coke deposits on fixed-bed catalysts by a radio frequency-based method, Sensors Actuators B 181 (2013) 681–689, http://dx.doi.org/10.1016/j.snb.2013.01.022, URL https://linkinghub.elsevier.com/retrieve/pii/S0925400513000294.

[47] J.L. Wheeler, N.P. Sullivan, J.M. Porter, Development of an impedance-based sensor for detection of catalyst coking in fuel reforming systems, Sensors Actuators B 183 (2013) 194–200, http://dx.doi.org/10.1016/j.snb.2013.03.084, URL https://linkinghub.elsevier.com/retrieve/pii/S0925400513003651.

[48] M. Lo Faro, S. Trocino, S. Zignani, A. Aricò, G. Maggio, C. Italiano, C. Fabiano, L. Pino, A. Vita, Study of a solid oxide fuel cell fed with n-dodecane reformate. Part I: Endurance test, Int. J. Hydrogen Energy 41 (13) (2016) 5741–5747, http://dx.doi.org/10.1016/j.ijhydene.2016.02.119, https://linkinghub.elsevier.com/retrieve/pii/S0360319915301373.

[49] N.S. Siefert, D. Shekhawat, M.W. Smith, D.J. Haynes, R.M. Bergen, E.H. Robey, R.S. Gemmen, D.A. Berry, Operation of a solid oxide fuel cell on a reformed FAME mixture, Biomass Bioenergy 47 (2012) 362–371, http://dx.doi.org/10.1016/j.biombioe.2012.09.024, URL https://linkinghub.elsevier.com/retrieve/pii/S0961953412003649.

[50] D. Ding, Z. Liu, L. Li, C. Xia, An octane-fueled low temperature solid oxide fuel cell with ru-free anodes, Electrochem. Commun. 10 (9) (2008) 1295–1298, http://dx.doi.org/10.1016/j.elecom.2008.06.026, URL https://linkinghub.elsevier.com/retrieve/pii/S1388248108002762.

[51] J. Lawrence, M. Boltze, Auxiliary power unit based on a solid oxide fuel cell and fuelled with diesel, J. Power Sources 154 (2) (2006) 479–488, http://dx.doi.org/10.1016/j.jpowsour.2005.10.036, URL https://linkinghub.elsevier.com/retrieve/pii/S0378775305014369.

[52] N. Kleinohl, P. Nehter, A. Bauschulte, J. Vom Schloß, J.B. Hansen, SOFC FED with European standard road diesel by an adiabatic prereforming fuel processor for 1000 hours, in: Proceedings of the 11th European SOFC and SOE Forum 2014, 2014, pp. 1–9, URL https://www.researchgate.net/publication/308919206.

[53] M. Reissig, J. Mathé, S. Planitzer, R. Vötter, J. Rechberger, Standalone portable SOFC power generator for autonomous operation, ECS Trans. 68 (1) (2015) 143–150, http://dx.doi.org/10.1149/06801.0143ecst, URL https://iopscience.iop.org/article/10.1149/06801.0143ecst.

[54] J. Rechberger, A. Kaupert, J. Hagerskans, L. Blum, Demonstration of the first European SOFC APU on a heavy duty truck, Transp. Res. Procedia 14 (2016) 3676–3685, http://dx.doi.org/10.1016/j.trpro.2016.05.442, URL https://linkinghub.elsevier.com/retrieve/pii/S2352146516304495.

[55] K. Sasaki, H.-W. Li, A. Hayashi, J. Yamabe, T. Ogura, S.M. Lyth, in: K. Sasaki, H.-W. Li, A. Hayashi, J. Yamabe, T. Ogura, S.M. Lyth (Eds.), Hydrogen Energy Engineering, in: Green Energy and Technology, Springer, Japan, Tokyo, 2016, http://dx.doi.org/10.1007/978-4-431-56042-5, URL http://link.springer.com/10.1007/978-4-431-56042-5.

[56] T. Nakao, S. Inoue, S. Uenoyama, Y. Takuwa, M. Suzuki, Progress of SOFC residential CHP system: Over 50,000 units market experience of osaka gas, ECS Trans. 91 (1) (2019) 43–49, http://dx.doi.org/10.1149/09101.0043ecst, URL https://iopscience.iop.org/article/10.1149/09101.0043ecst.

[57] S. Yoon, J. Bae, A diesel fuel processor for stable operation of solid oxide fuel cells system: I. Introduction to post-reforming for the diesel fuel processor, Catal. Today 156 (1–2) (2010) 49–57, http://dx.doi.org/10.1016/J.CATTOD.2010.01.006, URL https://www.sciencedirect.com/science/article/pii/S0920586110000076.

[58] Z. Pors, Energietechnik Energy Technology Eduktvorbereitung und Gemischbildung in Reaktionsapparaten zur autothermen Reformierung von dieselähnlichen Kraft-stoffen (Ph.D. thesis), 2006, p. 182.

[59] J. Lin, T.A. Trabold, M.R. Walluk, D.F. Smith, Bio-fuel reformation for solid oxide fuel cell applications. Part 1: Fuel vaporization and reactant mixing, Int. J. Hydrogen Energy 38 (27) (2013) 12024–12034, http://dx.doi.org/10.1016/j.ijhydene.2013.07.009, URL https://linkinghub.elsevier.com/retrieve/pii/S0360319913016819.

[60] X. Xu, P. Li, Y. Shen, Small-scale reforming of diesel and jet fuels to make hydrogen and syngas for fuel cells: A review, Appl. Energy 108 (2013) 202–217, http://dx.doi.org/10.1016/j.apenergy.2013.03.028, URL https://linkinghub.elsevier.com/retrieve/pii/S0306261913002249.

[61] J. Safarov, U. Ashurova, B. Ahmadov, E. Abdullayev, A. Shahverdiyev, E. Hassel, Thermophysical properties of diesel fuel over a wide range of temperatures and pressures, Fuel 216 (2018) 870–889, http://dx.doi.org/10.1016/J.FUEL.2017.11.125, URL https://www.sciencedirect.com/science/article/pii/S0016236117315399.

[62] Z. Navas-Anguita, D. García-Gusano, D. Iribarren, A review of techno-economic data for road transportation fuels, Renew. Sustain. Energy Rev. 112 (2019) 11–26, http://dx.doi.org/10.1016/j.rser.2019.05.041, URL https://linkinghub.elsevier.com/retrieve/pii/S1364032119303545.

[63] W. Sun, W. Huang, X. Qin, Y. Deng, Y. Kang, W. Peng, Y. Zhang, Z. Huang, Water impact on the auto-ignition of kerosene/air mixtures under combustor relevant conditions, Fuel 267 (2020) 117184, http://dx.doi.org/10.1016/j.fuel.2020.117184, URL https://linkinghub.elsevier.com/retrieve/pii/S0016236120301794.

[64] B. Wang, H. Olivier, H. Grönig, Ignition of shock-heated H2-air-steam mixtures, Combust. Flame 133 (1–2) (2003) 93–106, http://dx.doi.org/10.1016/S0010-2180(02)00552-7, URL https://linkinghub.elsevier.com/retrieve/pii/S0010218002005527.

[65] N. Donohoe, K.A. Heufer, C.J. Aul, E.L. Petersen, G. Bourque, R. Gordon, H.J. Curran, Influence of steam dilution on the ignition of hydrogen, syngas and natural gas blends at elevated pressures, Combust. Flame 162 (4) (2015) 1126–1135, http://dx.doi.org/10.1016/j.combustflame.2014.10.005, URL https://linkinghub.elsevier.com/retrieve/pii/S0010218014003149.

[66] G. Nusev, B. Morel, J. Mougin, Đ. Juričić, P. Boškoski, Condition monitoring of solid oxide fuel cells by fast electrochemical impedance spectroscopy: A case example of detecting deficiencies in fuel supply, J. Power Sources 489 (2021) http://dx.doi.org/10.1016/j.jpowsour.2021.229491.

[67] M. Gallo, C. Costabile, M. Sorrentino, P. Polverino, C. Pianese, Development and application of a comprehensive model-based methodology for fault mitigation of fuel cell powered systems, Appl. Energy 279 (2020) 115698, http://dx.doi.org/10.1016/j.apenergy.2020.115698, https://linkinghub.elsevier.com/retrieve/pii/S0306261920311934.

[68] V. Subotić, B. Stoeckl, V. Lawlor, J. Strasser, H. Schroettner, C. Hochenauer, Towards a practical tool for online monitoring of solid oxide fuel cell operation: An experimental study and application of advanced data analysis approaches, Appl. Energy 222 (2018) 748–761, http://dx.doi.org/10.1016/j.apenergy.2018.03.182, URL https://linkinghub.elsevier.com/retrieve/pii/S0306261918305324.

[69] P. Caliandro, A. Nakajo, S. Diethelm, J. Van herle, Model-assisted identification of solid oxide cell elementary processes by electrochemical impedance spectroscopy measurements, J. Power Sources 436 (2019) 226838, http://dx.doi.org/10.1016/j.jpowsour.2019.226838, https://linkinghub.elsevier.com/retrieve/pii/S0378775319308316.

[70] H. Sumi, H. Shimada, Y. Yamaguchi, T. Yamaguchi, Y. Fujishiro, Degradation evaluation by distribution of relaxation times analysis for microtubular solid oxide fuel cells, Electrochim. Acta 339 (2020) 135913, http://dx.doi.org/10.1016/j.electacta.2020.135913, https://linkinghub.elsevier.com/retrieve/pii/S0013468620303054.

[71] A. Weber, J. Szász, S. Dierickx, C. Endler-Schuck, E. Ivers-Tiffée, Accelerated lifetime tests for SOFCs, ECS Trans. 68 (1) (2015) 1953–1960, http://dx.doi.org/10.1149/06801.1953ecst, URL https://iopscience.iop.org/article/10.1149/06801.1953ecst.

[72] M. Ghamarinia, A. Babaei, C. Zamani, Electrochemical characterization of La2NiO4-infiltrated La0.6Sr0.4Co0.2Fe0.8O3-δ by analysis of distribution of relaxation times, Electrochim. Acta 353 (2020) 136520, http://dx.doi.org/10.1016/j.electacta.2020.136520, URL https://linkinghub.elsevier.com/retrieve/pii/S0013468620309130.

[73] V. Sonn, A. Leonide, E. Ivers-Tiffée, Combined deconvolution and CNLS fitting approach applied on the impedance response of technical Ni/8YSZ cermet electrodes, J. Electrochem. Soc. 155 (7) (2008) B675, http://dx.doi.org/10.1149/1.2908860, https://iopscience.iop.org/article/10.1149/1.2908860, https://iopscience.iop.org/article/10.1149/1.2908860/meta.

[74] Q. Fang, L. Blum, N.H. Menzler, Performance and degradation of solid oxide electrolysis cells in stack, ECS Trans. 68 (1) (2015) 3491–3503, http://dx.doi.org/10.1149/06801.3491ecst, URL https://iopscience.iop.org/article/10.1149/06801.3491ecst.

[75] R. O'Hayre, S.-W. Cha, W. Colella, F.B. Prinz, Fuel Cell Fundamentals, John Wiley & Sons, Inc, Hoboken, NJ, USA, 2016, http://dx.doi.org/10.1002/9781119191766, https://onlinelibrary.wiley.com/doi/book/10.1002/9781119191766, http://doi.wiley.com/10.1002/9781119191766.

[76] C. Song, Fuel processing for low-temperature and high-temperature fuel cells challenges, and opportunities for sustainable development in the 21st century, Catal. Today 77 (1–2) (2002) 17–49, http://dx.doi.org/10.1016/S0920-5861(02)00231-6, URL https://linkinghub.elsevier.com/retrieve/pii/S0920586102002316.

[77] J. Rechberger, M. Reissig, M. Hauth, AVL SOFC systems on the way of industrialization, ECS Trans. 57 (1) (2013) 141–148, http://dx.doi.org/10.1149/05701.0141ecst, URL https://iopscience.iop.org/article/10.1149/05701.0141ecst.

[78] R.U. Dietrich, J. Oelze, A. Lindermeir, C. Spitta, M. Steffen, T. Küster, S. Chen, C. Schlitzberger, R. Leithner, Efficiency gain of solid oxide fuel cell systems by using anode offgas recycle - results for a small scale propane driven unit, J. Power Sources 196 (17) (2011) 7152–7160, http://dx.doi.org/10.1016/j.jpowsour.2010.09.016.

[79] V. Saarinen, J. Pennanen, M. Kotisaari, O. Thomann, O. Himanen, S.D. Iorio, P. Hanoux, J. Aicart, K. Couturier, X. Sun, M. Chen, B.R. Sudireddy, Design, manufacturing, and operation of movable 2 × 10 kW size rSOC system, Fuel Cells (2021) http://dx.doi.org/10.1002/fuce.202100021, URL https://onlinelibrary.wiley.com/doi/10.1002/fuce.202100021.